

Wave heating from proto-neutron star convection and the core-collapse supernova explosion mechanism

Sarah E. Gossan,^{1,2,3*} Jim Fuller,² and Luke F. Roberts⁴

¹Canadian Institute for Theoretical Astrophysics, University of Toronto, Toronto, ON M5S 3H8, Canada

²TAPIR, Mailcode 350-17, California Institute of Technology, Pasadena, CA 91125, USA

³LIGO Lab, Mailcode 100-36, California Institute of Technology, 1200 E California Blvd, Pasadena, CA 91125, USA

⁴NSCL and Department of Physics and Astronomy, Michigan State University, East Lansing, MI 48824, USA

Accepted 2019 November 18. Received 2019 November 15; in original form 2019 October 16

ABSTRACT

Our understanding of the core-collapse supernova explosion mechanism is incomplete. While the favoured scenario is delayed revival of the stalled shock by neutrino heating, it is difficult to reliably compute explosion outcomes and energies, which depend sensitively on the complex radiation hydrodynamics of the post-shock region. The dynamics of the (non-)explosion depend sensitively on how energy is transported from inside and near the proto-neutron star (PNS) to material just behind the supernova shock. Although most of the PNS energy is lost in the form of neutrinos, hydrodynamic and hydromagnetic waves can also carry energy from the PNS to the shock. We show that gravity waves excited by core PNS convection can couple with outgoing acoustic waves that present an appreciable source of energy and pressure in the post-shock region. Using one-dimensional simulations, we estimate the gravity wave energy flux excited by PNS convection and the fraction of this energy transmitted upward to the post-shock region as acoustic waves. We find wave energy fluxes near 10^{51} erg s⁻¹ are likely to persist for ~ 1 s post-bounce. The wave pressure on the shock may exceed 10 per cent of the thermal pressure, potentially contributing to shock revival and, subsequently, a successful and energetic explosion. We also discuss how future simulations can better capture the effects of waves, and more accurately quantify wave heating rates.

Key words: convection – waves – stars: neutron – supernovae: general.

1 MOTIVATION

The core-collapse supernova (CCSN) explosion mechanism is not well understood. Several mechanisms have been proposed (see, e.g., Janka 2012; Janka et al. 2016; Müller 2016; Burrows et al. 2018 for broad reviews), but delayed shock revival through neutrino heating is favoured for progenitor cores with pre-collapse rotational periods greater than a few seconds (Bethe & Wilson 1985). The ability of the so-called delayed neutrino-heating mechanism to robustly drive energetic supernova explosions in a wide range of progenitor stars has yet to be fully established, although a subset of three-dimensional simulations are beginning to predict successful explosions for various progenitor stars (Janka et al. 2016; Ott et al. 2018; Burrows et al. 2020). What has become clear is that the development and sustained presence of multi-dimensional hydrodynamic instabilities in the post-shock accretion flow, such as turbulent neutrino-driven convection and the standing accretion-shock instability (SASI; see, e.g., Foglizzo et al. 2007 and references therein) is crucial for successful explosions. Even when explosions are produced, it is often not clear what the total explosion energy should

be, nor how it should be dependent on progenitor properties or the explosion dynamics.

The success or failure of the delayed neutrino-heating mechanism can be sensitive to small changes in the physics included in CCSN simulations, particularly to physics that effect the properties of the proto-neutron star (PNS; Melson et al. 2015; Bollig et al. 2017; Burrows et al. 2018; Schneider et al. 2019). Neutrino emission energising the shock in the pre-explosion phase is powered predominantly by accretion onto the PNS (Müller & Janka 2014), but this same accretion provides ram pressure which prevents shock runaway. This balance can be tilted in favour of explosion if the PNS is able to more efficiently couple the accretion power back to the post-shock region, for instance by increasing the average energy of the emitted neutrinos (e.g. Janka et al. 2016). Although accretion power provides the majority of the flux in electron neutrinos and anti-electron neutrinos prior to explosion, the potential for gravitational contraction of the inner regions of the PNS provides a huge reservoir of energy, totalling well over 10^{53} erg. Due to the relatively long diffusion timescale of neutrinos through the PNS, energy released through core contraction contributes a fairly small fraction of the total luminosity during the pre-explosion phase. Nevertheless, only ~ 5 per cent of the total neutrino luminosity is deposited in the

* E-mail: gossan@cita.utoronto.ca

gain region behind the stalled shock. Should another mechanism operate, one capable of transporting energy from the gravitational reservoir in the PNS core and depositing it in the post-shock region more efficiently than neutrinos, the energy released via gravitational contraction of the core could help to facilitate the delayed neutrino-heating mechanism.

Unsurprisingly, the long-term multineutrino energy group radiation hydrodynamic simulations required to explore the explosion mechanism continue to present a computationally daunting task. State-of-the-art simulations using three-flavour, multigroup neutrino radiation transport in multiple dimensions (see, e.g., [Lentz et al. 2015](#); [Melson et al. 2015](#); [Janka et al. 2016](#); [Roberts et al. 2016](#); [Vartanyan et al. 2019](#); [Burrows et al. 2019](#)) have seen some successful explosions, although less energetic than expected. While failed explosions are still seen with these more involved simulations, several studies have shown that the evolutionary track for many models exists near the boundary between successful explosion and failed supernova. It has been shown that modest changes to input physics and numerical techniques such as using more realistic input data for the progenitor models, can reduce the critical neutrino luminosity required for a successful explosion to develop ([Couch et al. 2015](#); [Abdikamalov et al. 2016, 2018](#)).

In the interest of reducing computational costs, a long-favoured tactic has been to employ a more coarsely spaced (i.e. lower resolution) radial grid. It has been shown, however, that failure to resolve turbulence across the inertial range of spatial scales reduces the turbulent pressure beneath the stalled shock, unintentionally further inhibiting explosions ([Abdikamalov et al. 2015](#); [Radice et al. 2015](#); [Couch & Ott 2015](#)). Additionally, this low resolution may impact the development of convection within the PNS. Another strategy used in some simulations is evolving part of the PNS in spherical symmetry (e.g. [Hanke et al. 2012](#); [Müller 2015a](#); [Müller et al. 2017](#)), which increases the Courant limit on the time-step. The elimination of non-radial hydrodynamics in the PNS, however, may suppress the development of convection there. PNS convection may efficiently transport energy out from the central regions of the PNS to near the neutrino decoupling radius, potentially increasing the emitted neutrino luminosities (e.g. [Dessart et al. 2006](#)) and exciting outgoing internal gravity waves above the PNS.

Generally speaking, the impact of the approximations highlighted above on the “explodability” of realistic progenitor stars is only beginning to be understood. As a consequence, it is important to investigate the significance of additional physical processes (or “mechanisms”) contributing to the dynamics of shock revival, even if they are sub-dominant.

In this paper, we seek to explore the effect of heating from gravito-acoustic waves excited by PNS convection on shock revival and explosion energy in the context of CCSNe. In the following, we outline the basic concept of our proposed idea in Section 2, detail the one-dimensional simulations employed for this study in Section 3, and describe our calculations of the wave energy fluxes in Section 4. In Section 5, we examine wave damping processes and the impact of non-linear wave dynamics, before discussing the implications (and limitations) of our work in light of these effects in Section 6, and concluding with Section 7.

2 BASIC IDEA

The evolution of the PNS and supernova shock wave during the first few hundred milliseconds after core bounce is, for the most part, agreed upon by simulations ([O’Connor et al. 2018](#)). The shock’s

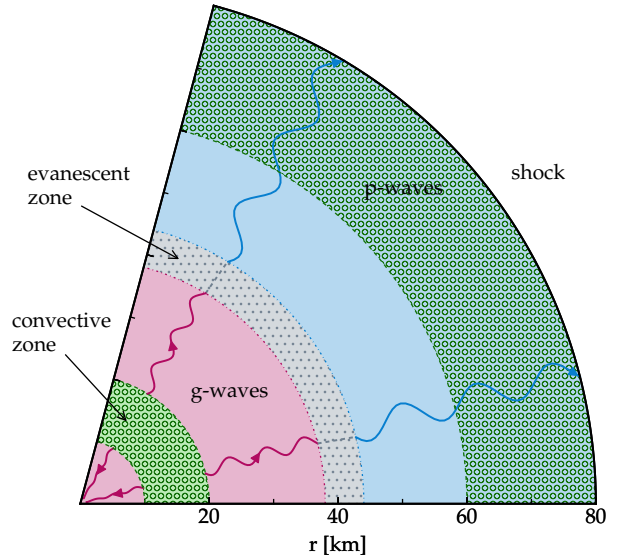


Figure 1. Gravity waves are excited by turbulent convection (green hatched regions) in the PNS and propagate outward (pink regions). At evanescent zones (grey region), the waves either reflect back towards the PNS, or they tunnel through the evanescent region to generate outgoing acoustic waves. These waves propagate outwards until they are damped or they encounter the shock, beyond which they cannot propagate. Both wave pressure on the shock and dissipation of wave energy in the gain region may aid shock revival.

energy is drained through a combination of neutrino losses and photodissociation of infalling heavy nuclei, and the shock wave stalls (at radius r_{shock}) between 150 and 250 km. The subsonic material interior to (beneath) the shock is roughly in hydrostatic equilibrium. Within ~ 100 ms of core bounce, regions of net neutrino heating (in the post-shock “gain region”) and net neutrino cooling (above the PNS neutrinosphere, roughly located around density $\rho \sim 10^{11} \text{ g cm}^{-3}$) develop. The negative entropy gradient that emerges in the gain region drives vigorous convection there which rapidly becomes turbulent. The gain radius, marking the inner bound of the net heating region beneath the stalled shock, is typically between 50 and 100 km. Beneath the gain region exists a radiative layer that is stably stratified through net neutrino cooling that creates a positive entropy gradient. This layer extends below the neutrinosphere, interior to which neutrinos are strongly coupled to (i.e. trapped by) the dense nuclear matter comprising the inner PNS core. Meanwhile, gradients in composition and entropy develop between the hot, lepton-rich core and the neutrino-cooled, deleptonized neutrinospheres, driving convection in the PNS mantle. Many simulations confirm the development a convective layer in the PNS mantle within 150 to 200 ms after core bounce, at radii between roughly 10 and 20 km (e.g. [Dessart et al. 2006](#)).

We are concerned with the effects of energy transport via hydrodynamic waves from the PNS mantle out to the post-shock region. As discussed by [Goldreich & Kumar \(1990\)](#), internal gravity waves are generated by turbulent convection and emitted at convective-radiative interfaces, transporting energy and angular momentum away from the convective zone, and depositing it where the waves damp away. Energy and angular momentum transport through gravity waves generated via this mechanism can be significant, and has been shown to have important ramifications inside low-mass, Sun-like stars (e.g. [Kumar et al. 1999](#); [Talon et al. 2002](#); [Fuller et al. 2014](#)), intermediate-mass stars (e.g. [Rogers et al. 2012](#),

2013), and massive stars (see, e.g., Meakin & Arnett 2007; Quataert & Shiode 2012; Fuller et al. 2015b; Fuller 2017).

In the context of the PNS and the evolving supernova shock, gravity waves are expected to be excited in two regions; the optically thick and convective PNS mantle, and secondly in the gain region below the shock due to neutrino-driven convection. The detailed study of Dessart et al. (2006) (see also Yoshida et al. 2007) examines the properties of the inner PNS convection zone and the gravity waves in the overlying radiative (neutrino-cooled) layer. They find gravity waves with angular index $\ell = 1 - 3$ and frequencies of $\omega \sim 10^3 \text{ rad s}^{-1}$ are prevalent, though they attribute their excitation primarily to the (more vigorous) convection in the outer convective zone. We note, however, that gravity waves are also excited by the convection zone in the PNS mantle. Gravity waves generated here will couple to acoustic waves in the outer PNS, where they then propagate out towards the stalled shock. Energy and angular momentum is transported outwards by these waves from the convective zone in the PNS mantle (which is driven, ultimately, by the release of gravitational binding energy as the nascent remnant cools and contracts over the time-scale of a few seconds), and deposited in regions of heavy damping. Should this damping occur predominantly in the gain region, the increased energy deposition may augment the thermal pressure behind the shock, and aid in its revival. Alternatively, waves that propagate all the way to the shock will be reflected back inwards, contributing an additional source of pressure upon the shock to drive it outwards. We illustrate this scenario in Fig. 1 with a stylised cartoon diagram.

We note that this process is related to the ‘‘acoustic mechanism’’ proposed by Burrows et al. (2006a), but with key differences. While the former is powered by energy from accretion of infalling material onto the outer PNS, the acoustic energy we consider comes from the liberation of gravitational binding energy as the PNS core deleptonizes and contracts. This reservoir, containing well over 10^{53} erg of binding energy at capacity, remains tappable long after accretion onto the PNS has ceased. Consequently, gravity waves excited in this way have the potential to aid shock revival and help to drive the explosion for several seconds after core bounce. The transport of a small fraction of the PNS binding energy out to the gain region via gravity waves may be considered an aspect of the so-called CCSN ‘‘central engine’’. It follows that effects from these waves may be missed in simulations that (for the purposes of reducing computational cost) do not follow PNS evolution either (i) long enough to witness the development of a convective layer in the PNS mantle, or (ii) with sufficient degrees of freedom in long-running simulations, suppressing the development of non-radial hydrodynamic instabilities and, in turn, their effect. Even in simulations that may capture these waves, their impact on the explosion mechanism has not been explicitly noted and quantified.

First and foremost, the goal of the study presented here is to determine the extent to which gravito-acoustic waves generated by PNS convection could contribute to shock revival. This could increase the fraction of explosions seen by simulations evolving CCSNe, as well as the characteristic explosion energies. We employ spherically symmetric simulations to estimate the spectral behaviour and energy flux of waves excited by PNS convection, then quantitatively estimate heating rates in the gain region from wave energy transport for the first 660 ms after core bounce. We discuss the assumptions made to calculate these estimates, and explore how wave damping and non-linear effects could impact our results. Lastly, we consider how wave dynamics can be captured and heating rates quantified in future simulations.

3 SIMULATIONS

We employ a spherically symmetric, fully implicit, general relativistic radiation hydrodynamics code, which employs mixing length theory to account for the effect of convective energy transport (Roberts 2012a,b). Neutrino transport is treated through a general-relativistic moment-wise scheme, employing a variable Eddington factor approach which retains only the first two moment equations and assumes a closure relation between these and higher order moments (see Mihalas & Weibel-Mihalas 1984) derived from a formal solution of the static relativistic Boltzmann equation (Roberts 2012b). The approach, which incorporates inelastic scattering and pair production, treats the spectral behaviour of the neutrinos via energy-integrated groups. Three species of neutrino are considered, $\nu_i \in \{\nu_e, \bar{\nu}_e, \nu_x\}$, where ν_x is a characteristic heavy-lepton neutrino employed to encompass the effects of neutrinos ν_μ , ν_τ , and their antiparticles. Each neutrino population is modelled by a distribution of massless fermions, where neutrinos within a given energy bin are distributed as for a Fermi blackbody. For each energy group, the effective Planck mean opacity from absorption is computed using a 10-point quadrature to calculate the group-averaged opacities, corrected for detailed balance. Group-averaged opacities from scattering, calculated using a five-point quadrature, are not weighted by the local thermal neutrino distribution.

We simulate the core collapse and post-bounce evolution of a $15 M_\odot$ progenitor star from Woosley & Weaver (1995) out to 660 ms after core bounce. To close the set of general-relativistic radiation hydrodynamic equations, we employ the Lattimer-Swesty equation of state with incompressibility parameter $K = 220 \text{ MeV}$, modified as outlined in Lattimer & Douglas Swesty (1991) and Schneider et al. (2017). The prescription for energy-dependent neutrino transport uses 20 energy groups covering $[0, 200] \text{ MeV}$. Here, 19 logarithmically spaced energy bins span the range $[0, 80] \text{ MeV}$, and a final group spans $[80, 200] \text{ MeV}$. In Fig. 2, we show snapshots of the radial profiles of interior PNS quantities at 225, 349, 475, and 599 ms after core bounce.

The entropy in the post-shock region rises from $\sim 12 k_B \text{ baryon}^{-1}$ to $\sim 22 k_B \text{ baryon}^{-1}$ between 225 and 600 ms after core bounce. Gradients in composition and temperature in the PNS mantle steepen with time, driving convective instability there from $\sim 200 \text{ ms}$ after core bounce through the end of the simulation. The peak temperature, located around the inner boundary of the inner convective zone, rises from $\sim 30 \text{ MeV}$ to more than 50 MeV between 225 and 660 ms as the PNS cools and contracts. Comparatively, low lepton fractions in the PNS core are accompanied by strongly degenerate ν_e neutrinos. In the domain $10 \text{ km} \lesssim r \lesssim 20 \text{ km}$, convection is driven by negative lepton and entropy gradients, with convective transport pushing the unstable region towards neutral buoyancy.

4 WAVE GENERATION AND ENERGY TRANSPORT

Gravity waves are excited by turbulent convection at the interface between convective and radiative zones. To establish said boundaries, we use the sign of the squared Brunt-Väisälä (or buoyancy) frequency N^2 as a proxy for the convective stability of a particular region, where

$$N^2 = -\frac{g}{n_B} \left(\frac{dn_B}{dr} - \frac{dP}{dr} \left(\frac{\partial n_B}{\partial P} \right)_s \right), \quad (1)$$

given the local gravitational acceleration g and number density of baryons n_B . We designate radial grid zones convective where $N^2 < 0$, and conversely radiative grid zones where $N^2 > 0$. For

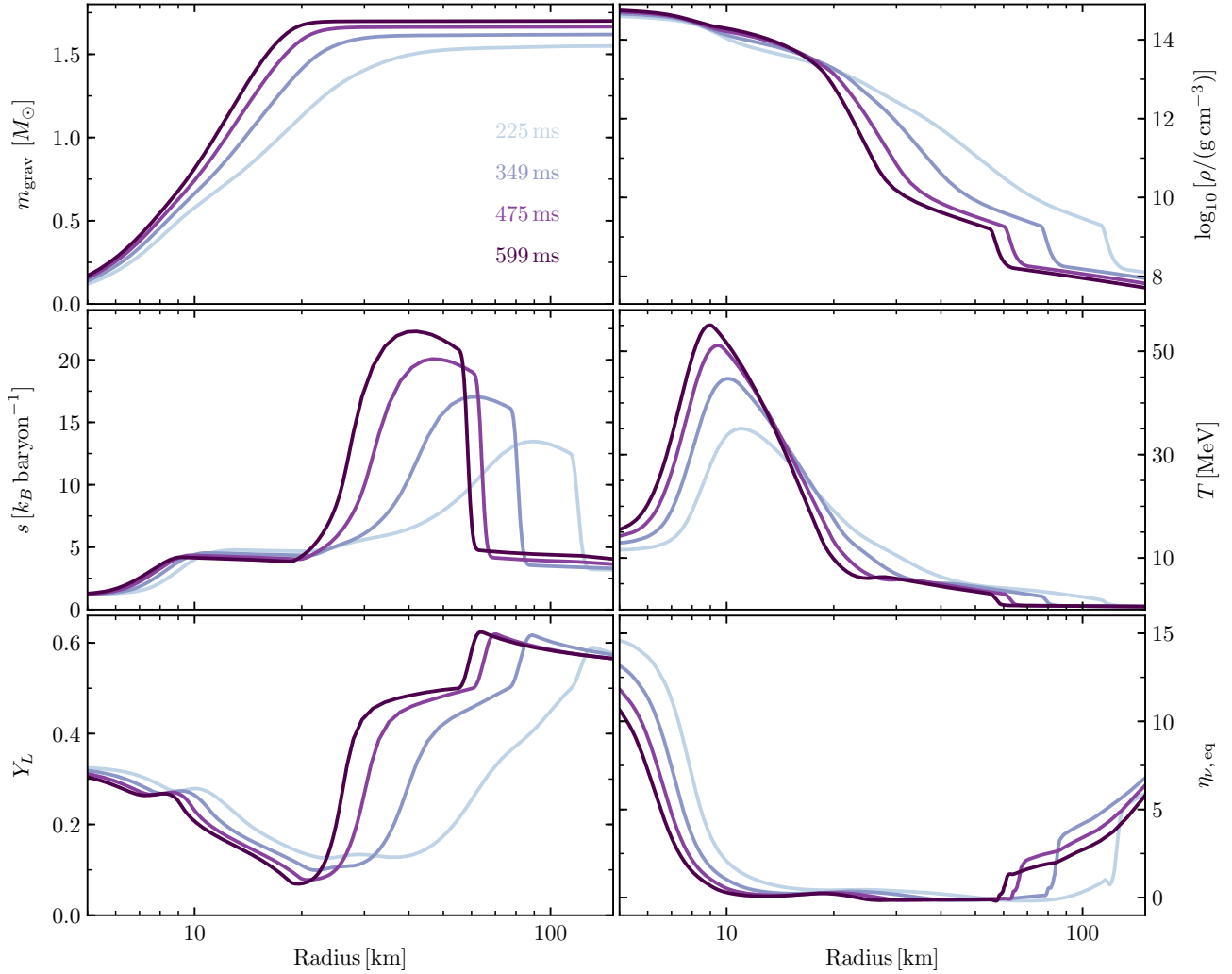


Figure 2. Radial profiles of the enclosed gravitational mass m_{grav} (top left-hand panel), logarithmic mass density $\log_{10}\rho$ (top right-hand panel), specific entropy s (centre left-hand panel), temperature T (centre right-hand panel), lepton fraction Y_L (bottom left-hand panel), and neutrino degeneracy parameter $\eta_{\nu, \text{eq}}$ (bottom right-hand panel) inside the PNS at four times after core bounce. Snapshots at 225, 349, 475, and 599 ms are shown in light blue, lavender, rich lilac, and aubergine, respectively.

plotting purposes, the scaled buoyancy frequency N_p is also an instructive quantity to calculate, where

$$N_p = \text{sign}(N^2) \sqrt{|N^2|}. \quad (2)$$

In the top panel of Fig. 3, we show the temporal evolution of N_p below the shock. We see the emergence of a convectively unstable region around 20 km a little before 200 ms after bounce, which quickly develops into a convective layer between 10 and 20 km that persists through the end of our simulation. We note that, in the region of interest (the outer boundary of the inner convective region), N_p is of order $\sim 10^3 \text{ rad s}^{-1}$.

The emitted flux in gravity waves L_{waves} is a small fraction of the convective energy flux L_{con} . While there is some uncertainty in the wave spectrum and energy flux, both analytic (Goldreich & Kumar 1990; Lecoanet & Quataert 2013) and numerical work (Couston et al. 2018) suggest the wave energy flux is approximately

$$L_{\text{waves}} \sim \mathcal{M}_{\text{con}} L_{\text{con}}, \quad (3)$$

where the convective Mach number $\mathcal{M}_{\text{con}} = v_{\text{con}}/c_s$ can be calcu-

lated using the characteristic convective velocity

$$v_{\text{con}} = \left[\frac{L_{\text{con}}}{4\pi r^2 \rho} \right]^{1/3}. \quad (4)$$

In practice, we can use the total outgoing neutrino luminosity L_ν to estimate v_{con} as, in the optically thick inner PNS where convection is efficient and carries almost all of the energy flux, $L_{\text{con}} \sim L_\nu$. For the purposes of this study, we employ L_{waves} as estimated at the upper edge of the inner convective region, where we expect the waves to emerge. In the bottom panel of Fig. 3, we show the evolution of L_{waves} across the inner convective zone with time. At the upper edge, we see wave luminosities in excess of $10^{51} \text{ erg s}^{-1}$ sustained from around 200 ms after core bounce through the end of our simulation.

We consider waves generated by convective motion within a pressure scale height H_p of the outer boundary of the inner convective region (at radius $r = r_{\text{con}}$), where

$$H_p = \frac{P}{g(\rho + P/c^2)}. \quad (5)$$

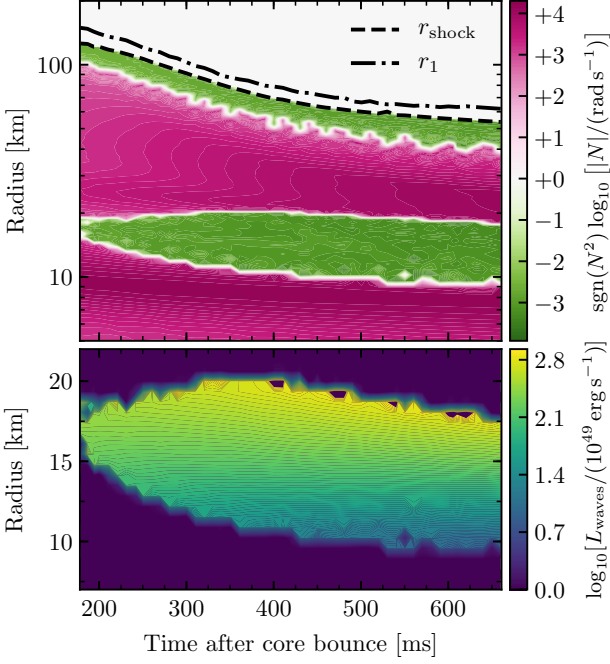


Figure 3. (Top panel) Colormap showing the time evolution of the scaled Brunt-Väisälä frequency $N_p = \text{sign}(N^2)\sqrt{|N^2|}$ (units of 10^3 rad s^{-1}) as a function of radius r between 200 ms and 660 ms after core bounce. The shock front is bounded by inner radius r_{shock} (shown with dashed black line) and outer radius r_1 (shown with dot-dashed black line). Convectively unstable regions ($N_p < 0$) are shown in green, while radiative regions ($N_p > 0$, where gravity waves can propagate), are shown in pink. (Bottom panel) Temporal evolution of the characteristic wave luminosity $L_{\text{waves}} = M_{\text{con}} L_{\text{con}}$ generated by turbulent convection in the inner convective region.

While the frequency and angular wavenumber spectra of waves generated in this scenario are decidedly uncertain (Lecoanet & Quataert 2013; Rogers et al. 2013; Alvan et al. 2014; Couston et al. 2018), most literature agrees that the wave power drops significantly at frequencies above the local convective turnover frequency ω_{con} , which we define as

$$\omega_{\text{con}} = \frac{\pi v_{\text{con}}}{2H_p}. \quad (6)$$

We adopt a flat spectrum across angular modes $\ell \in [1, \dots, \ell_c]$, where $\ell_c = r_{\text{con}}/\Delta r_{\text{con}}$ is determined by the physical width of the convection zone, Δr_{con} . This choice reflects the fact that thin convective zones have smaller eddies that excite waves with smaller horizontal wavelength and thus larger angular wavenumber ℓ . The emitted wave flux per mode $L_{\text{waves}, \ell}$ is then just

$$L_{\text{waves}, \ell} = \frac{L_{\text{waves}}}{\ell_c}. \quad (7)$$

In Fig. 4, we show the evolution of the convective velocity v_{con} , convective turnover frequency ω_{con} , maximum angular wavenumber excited ℓ_c , and the wave flux per angular mode $L_{\text{waves}, \ell}$ with time. We find the convective velocity remains roughly constant around $v_{\text{con}} \sim (4 - 4.5) \times 10^8 \text{ cm s}^{-1}$, while the convective turnover frequency steadily increases by a factor of roughly four from $\omega_{\text{con}} \sim 10^3 \text{ rad s}^{-1}$ to $\omega_{\text{con}} \sim 4 \times 10^3 \text{ rad s}^{-1}$ between 200 ms post-bounce through the end of our simulation. At early times, when the physical width of the inner convective zone is small, modes up to $\ell_c \sim (5 - 6)$ are excited, though $\ell_c \lesssim 3$ by ~ 250 ms post-bounce. From ~ 250 ms through the end of our simulation, the emitted wave luminosity per angular mode exceeds $10^{51} \text{ erg s}^{-1}$.

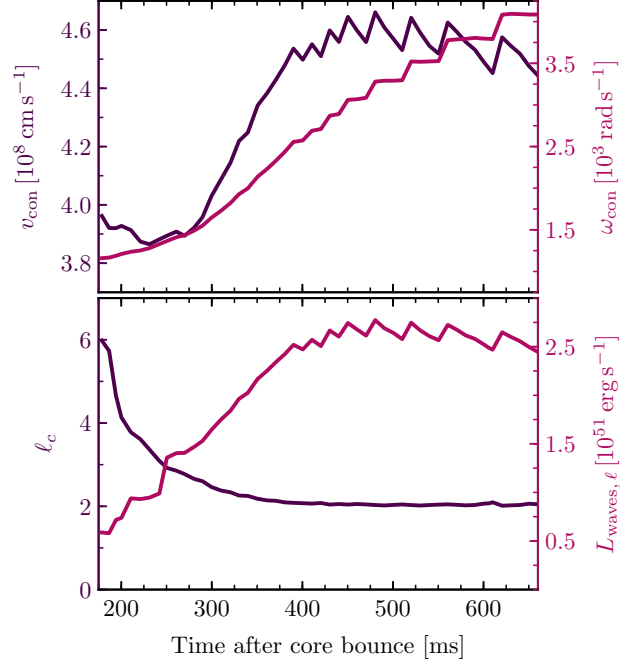


Figure 4. (Top panel) The evolution of the convective velocity v_{con} (left axis, deep purple line) and convective turnover frequency ω_{con} (right axis, deep pink line) at the upper edge of the inner convective region with time. (Bottom panel) The evolution of the maximum angular wave mode excited ℓ_c (left axis, deep purple line) and emitted wave luminosity per excited angular mode ℓ , $L_{\text{waves}, \ell}$ (right axis, deep pink line) near the upper edge of the inner convective region are shown with time.

After waves are excited, their propagation within the PNS is largely governed by the dispersion relation for gravitoacoustic waves of angular frequency ω . In the WKB approximation (see, e.g., Eq. S7 in (Fuller et al. 2015a)), the radial wavenumber $k_{r, \ell}$ for waves of angular mode ℓ is

$$k_{r, \ell}^2 = \frac{(|N|^2 - \omega^2)(L_\ell^2 - \omega^2)}{\omega^2 c_s^2}, \quad (8)$$

where Lamb frequencies L_ℓ are defined

$$L_\ell^2 = \frac{\ell(\ell+1)c_s^2}{r^2}, \quad (9)$$

given adiabatic sound speed $c_s^2 = \Gamma_1 P/\rho$, where $\Gamma_1 = (\partial \log P/\partial \log \rho)_s$ is the adiabatic index. Where $\omega < N, L_\ell$, the waves propagate as gravity waves, while they propagate as acoustic waves where $\omega > N, L_\ell$. Where $N < \omega < L_\ell$ and $L_\ell < \omega < N$, waves cannot propagate and are evanescent. In Fig. 5, we show propagation diagrams for $\ell = 2$ waves at 225 ms, 349 ms, 475 ms, and 599 ms after core bounce. From Fig. 5, we see that the width of the evanescent region is highly sensitive to the wave frequency. For $\ell = 2$ waves, the propagation track along $\omega = \omega_{\text{con}}$ skims the bottom of a large evanescent region in frequency space. After one pass, a fraction T_ℓ^2 of the incident wave flux is transmitted through the evanescent region (bounded by gravitoevanescent radius $r_{\text{grav-ev}}$ and acoustic-evanescent radius $r_{\text{ac-ev}}$), where transmission coefficients T_ℓ are

$$T_\ell = \exp \left[- \int_{r_{\text{grav-ev}}}^{r_{\text{ac-ev}}} dr |k_\ell| \right]. \quad (10)$$

While, in principle, more wave energy could leak through the

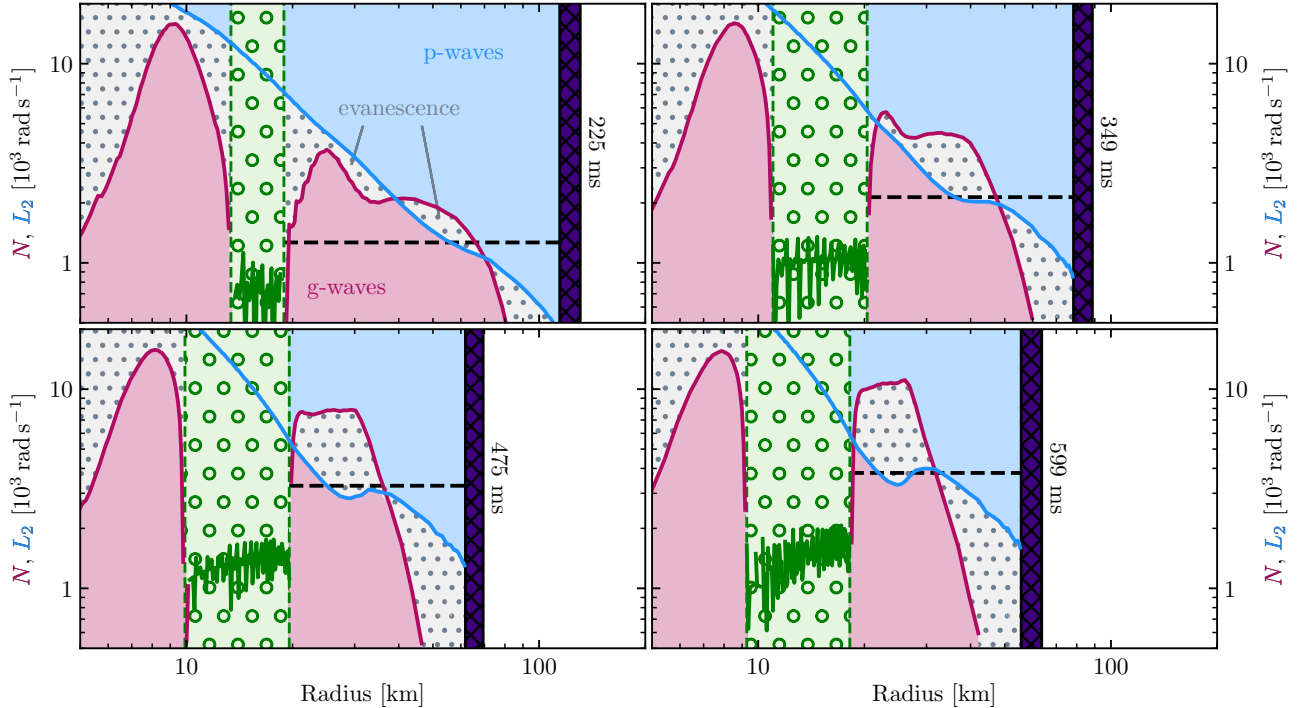


Figure 5. Propagation diagrams for $\ell = 2$ gravitoacoustic waves at 225 ms (top left-hand panel), 349 ms (top right-hand panel), 475 ms (bottom left-hand panel), and 599 ms (bottom right-hand panel) after core bounce. In each panel, the inner convective region is shown with green shading with circle hatch, with the magnitude of the scaled buoyancy frequency $|N_p|$ overlaid. The $\ell = 2$ Lamb frequency L_2 is shown in blue and, in radiative regions, the scaled buoyancy frequency N_p is shown in deep pink. Regions where gravity waves of angular frequency ω can propagate (i.e., where $\omega < N, L_2$) are shaded in pink, while regions in which acoustic waves can propagate (i.e., where $\omega > N, L_2$) are shaded in blue. Waves cannot propagate in evanescent regions (where $N < \omega < L_2$ or $N > \omega > L_2$), shown with grey shading and dotted hatch. The physical extent of the shock is indicated with dark purple shading and crossed hatch. For waves at frequency ω_{con} , the propagation track is shown with a thick dashed black line.

boundary following multiple reflections within the PNS, we adopt $L_{\text{trans}, \ell} = L_{\text{waves}, \ell} T_{\ell}^2$ as a conservative lower limit on the wave flux in angular mode ℓ entering the outer PNS.

In Fig. 6, we show snapshots of T_{ℓ}^2 , the fraction of wave energy transmitted out to the post-shock region, for $\ell = 1 - 3$ waves as a function of angular frequency at 225 ms, 349 ms, 475 ms, and 599 ms after core bounce. We see that uncertainty in ω_{con} translates to uncertainties of order unity in the wave flux transmitted through the evanescent region. In reality, a spectrum of waves extending above and below ω_{con} will be generated, and the energy transmitted into acoustic waves of wavenumber ℓ will be $\int d\omega T_{\ell}^2 (dL_{\text{waves}, \ell} / d\omega)$, where $(dL_{\text{waves}, \ell} / d\omega)$ is the energy flux in waves generated per unit frequency ω . As the wave spectrum is uncertain, this integral is uncertain, but Fig. 6 demonstrates that we expect transmission fractions of order $T_{\ell}^2 \sim 0.3$, dependent on the excited wave spectrum and time after core bounce.

Following their transmission out the upper edge of the evanescent region, acoustic waves can travel almost unimpeded out to the shock. The wave energy transport rate (i.e., “transmission rate”) beyond the last evanescent region encountered is given by

$$L_{\text{trans}} = \sum_{\ell=1}^{\ell_c} L_{\text{trans}, \ell}, \quad (11)$$

$$L_{\text{trans}, \ell} = L_{\text{waves}, \ell} T_{\ell}^2. \quad (12)$$

We show the temporal evolution of the transmitted wave power for $\ell = 1 - 3$ angular modes and the summed total in the post-shock region in Fig. 7. Once the inner PNS convection zone forms and

begins generating waves, we find net transmitted wave power L_{trans} in excess of $\sim 10^{51}$ erg s $^{-1}$ through the end of our simulation. The power contributed by $\ell = 1$ waves drops significantly with time, with transmitted power in $\ell = 2$ and $\ell = 3$ waves responsible for most of the net heating in the post-shock region. As illustrated by Fig. 6, a more accurate calculation that integrates over the wave spectrum may change the transmission profile. For example, at 349 ms post-bounce (as shown in the top right-hand panel of Fig. 6), we see that lower frequency $\ell = 1$ waves and higher frequency $\ell = 3$ waves would be transmitted more easily. While this might yield slightly different net wave power transmission rates, we expect our results to be accurate within a factor of order unity.

5 WAVE DAMPING AND NON-LINEAR EFFECTS

Until now, our calculations have implicitly assumed that waves generated by PNS convection propagate according to linear perturbation theory, and we have ignored sources of damping. We now address the validity of these assumptions, and work to quantify the effect of wave damping and non-linearity.

5.1 Neutrino damping

As discussed in Weinberg & Quataert (2008), gravity wave attenuation through radiative losses is dominated by increased neutrino emission from regions of wave compression. Here, we consider the

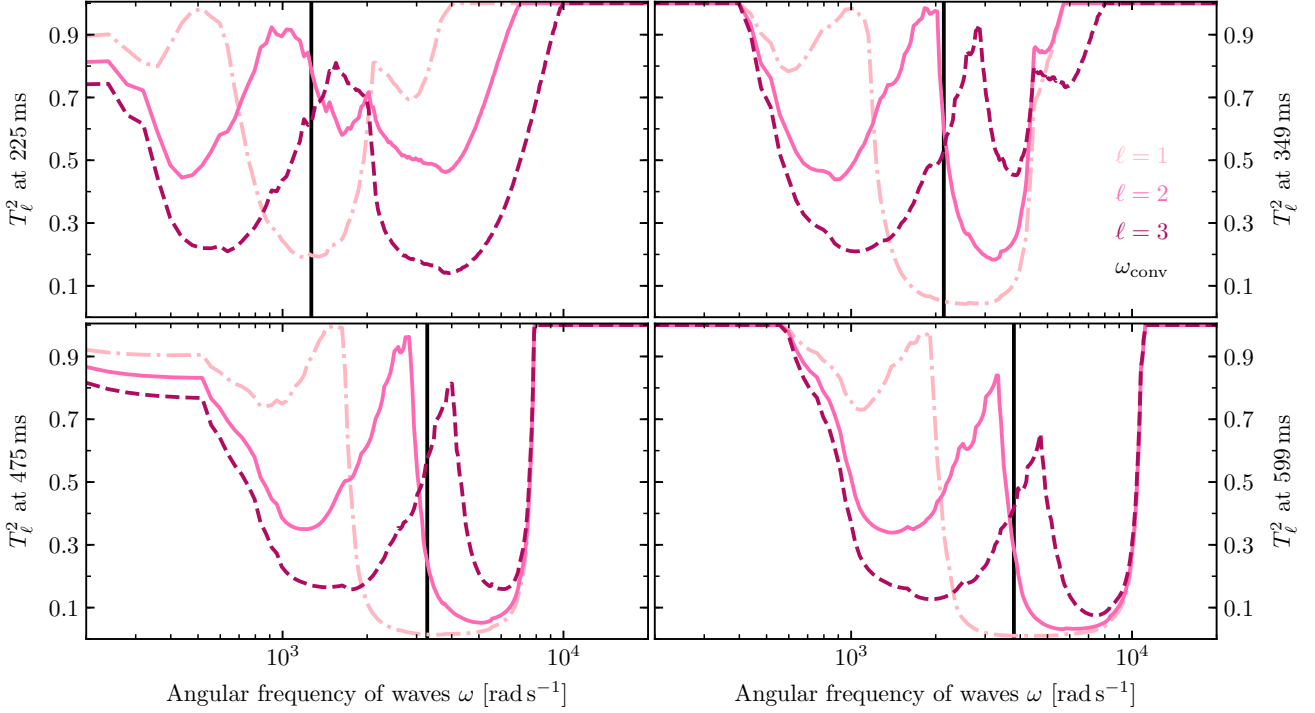


Figure 6. (Top left-hand panel) Snapshots of the squared transmission coefficients T_ℓ^2 for $\ell = 1$ (dash-dotted light pink line), $\ell = 2$ (solid hot pink line), and $\ell = 3$ (dashed deep pink line) waves as a function of angular wave frequency ω at 225 ms post-bounce. The convective turnover frequency ω_{con} , at which we assume waves are excited, is indicated with a solid black line. Similar snapshots at 349 ms (top right-hand panel), 475 ms (bottom left-hand panel), and 599 ms (bottom right-hand panel) post-bounce are shown.

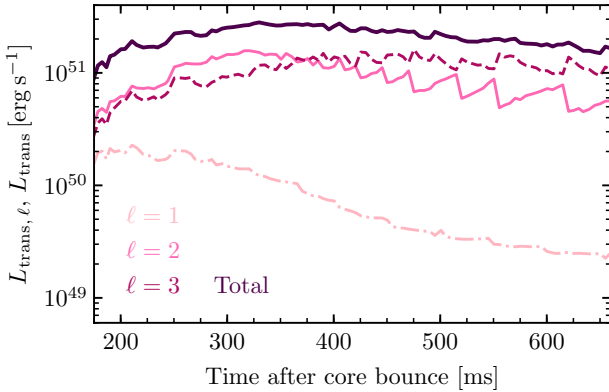


Figure 7. Temporal evolution of the transmitted wave power $L_{\text{trans},\ell}$ for $\ell = 1$ (light pink dash-dotted line), $\ell = 2$ (solid hot pink line), and $\ell = 3$ (dashed deep pink line) waves in the post-shock region following core bounce. The total transmitted wave power L_{trans} , summed over all excited wave modes, is overlaid with a thick deep purple line.

neutrino damping of gravity waves emitted from the inner convective zone as they propagate from the PNS core out to the stalled shock.

The energy loss rate from neutrino damping, $\dot{\epsilon}_\nu$, can be calculated as

$$\dot{\epsilon}_\nu = \delta T \delta \left(\frac{ds}{dt} \right)_\nu, \quad (13)$$

where δ denotes the Lagrangian variation of the following term, and ds/dt is the rate of change of specific entropy due to neutrino dissipation. While accurately calculating $\delta(ds/dt)_\nu$ in the neutrino

decoupling region requires a full solution of the neutrino transport equations, we can consider in turn the limits of optically thick damping (where wavelength $\lambda_{r,\ell} \sim 2\pi/|k_{r,\ell}|$ exceeds the neutrino mean free path $\langle d_{\nu_i} \rangle$) and optically thin damping ($\lambda_{r,\ell} < \langle d_{\nu_i} \rangle$) to simplify matters considerably.

In the optically thick limit, neutrino losses are dominated by the diffusion of μ and τ neutrinos, for which the mean free path is determined pre-dominated by neutral current scattering on nucleons. It can be shown (see Section A1) that

$$\dot{\epsilon}_{\nu,\text{thick}} \approx \frac{c (k_B m_e c^2)^2 |k_{r,\ell}|^2 \delta T^2}{9 (\hbar c)^3 \sigma_0 n_B^2 C(Y_e)}, \quad (14)$$

where $\sigma_0 = 1.7 \times 10^{-44} \text{ cm}^2$ is the fiducial weak interaction cross section, and

$$C(Y_e) = \frac{1 + 5g_A^2}{6} \frac{1 - Y_e}{4} + \frac{(C'_V - 1)^2 + 5g_A^2 (C'_A - 1)^2}{6} Y_e, \quad (15)$$

encompasses compositional effects. Here, $g_A \approx -1.27$ is the charged current axial coupling constant, while $C'_A = 0.5$ and $C'_V \approx 0.96$ are the neutral current axial and vector coupling constants, respectively.

Conversely in the optically thin limit, neutrino losses are dominated by emission and subsequent free-streaming of ν_e and $\bar{\nu}_e$ neutrinos, which is driven by charged-current capture on nucleons. In this scenario, the energy loss rate in neutrinos can be shown (see Section A2) to take the form;

$$\dot{\epsilon}_{\nu_e + \bar{\nu}_e, \text{thin}} \approx \frac{3c\sigma_0 k_B^6}{4\pi^2 (\hbar c)^3 (m_e c^2)^2} C_{\nu_e + \bar{\nu}_e, \text{thin}} T^4 \delta T^2, \quad (16)$$

where, we have defined

$$C_{\nu_e + \bar{\nu}_e, \text{thin}} = (1 + 3g_A^2) \times \left[Y_e \int_{\Delta_{np}/T}^{\infty} dx x^5 \left(1 - \frac{\Delta_{np}}{xT}\right)^2 \frac{1 + e^{-x - \eta_{\nu_e, \text{eq}}}}{1 + e^{x + \eta_{\nu_e, \text{eq}}}} + (1 - Y_e) \int_0^{\infty} dx x^5 \left(1 + \frac{\Delta_{np}}{xT}\right)^2 \frac{1 + e^{-x + \eta_{\nu_e, \text{eq}}}}{1 + e^{x - \eta_{\nu_e, \text{eq}}}} \right], \quad (17)$$

to encompass coupling constants and compositional effects.

Requiring continuity in the energy damping rates between the optically thick and optically thin limits, we may define some critical wavenumber k_{crit} such that

$$\dot{\epsilon}_{\nu, \text{thick}} (k = k_{\text{crit}}) = \dot{\epsilon}_{\nu, \text{thin}} (k = k_{\text{crit}}). \quad (18)$$

Using the expressions derived above, we find

$$k_{\text{crit}} = \frac{3\sigma_0 n_B (k_B T)^2}{2\pi(m_e c^2)^2} \sqrt{3C(Y_e) C_{\nu_e + \bar{\nu}_e, \text{thin}}}. \quad (19)$$

Given this threshold, we treat wave damping via neutrino dissipation in the optically thick limit where $k < k_{\text{crit}}$, and conversely in the optically thin limit where $k > k_{\text{crit}}$.

For waves with angular frequency ω , the damping frequency ω_{damp} is defined

$$\omega_{\text{damp}} \equiv \frac{\dot{\epsilon}_{\nu}}{\epsilon_{\text{wave}}}, \quad (20)$$

where $\epsilon_{\text{wave}} \sim \omega^2 |\xi|^2$ is the wave energy per unit mass, and $|\xi|$ is the magnitude of the wave displacement.

The Lagrangian temperature perturbation produced under passage of the wave is given by

$$\frac{\delta T}{T} \sim |k_{r, \ell}| \xi_r, \quad (21)$$

where ξ_r is the radial component of the wave displacement. For gravity waves, $\xi_r \sim (\omega/|N|) |\xi|$, while $\xi_r \sim |\xi|$ for acoustic waves. The damping frequency may then be expressed more generally as

$$\omega_{\text{damp}} \approx \frac{|k_{r, \ell}|^2}{\omega^2} \min \left[1, \frac{\omega^2}{|N|^2} \right] \times \begin{cases} \frac{c (k_B m_e c^2)^2}{9 (\hbar c)^3 \sigma_0} \frac{|k_{r, \ell}|^2}{n_B^2 C(Y_e)} T^2 & k \leq k_{\text{crit}}, \\ \frac{3c \sigma_0 k_B^6}{4\pi^2 (\hbar c)^3 (m_e c^2)^2} C_{\nu_e + \bar{\nu}_e, \text{thin}} T^6 & k > k_{\text{crit}}. \end{cases} \quad (22)$$

By incorporating the neutrino energy loss term into the energy evolution equation, one can show that it causes the wave frequency ω to become imaginary with damping rate γ_{ν} . In the quasi-adiabatic limit where $\gamma_{\nu} \ll \omega$, the wave amplitude damping rate is

$$\gamma_{\nu} \approx \frac{1}{2} \omega_{\text{damp}}, \quad (23)$$

while in the isothermal limit (where heat diffusion is fast), we find

$$\gamma_{\nu} \approx \frac{1}{2} \frac{\omega^2}{\omega_{\text{damp}}}. \quad (24)$$

Generally speaking, the wave damping rate may be written

$$\gamma_{\nu} \approx \frac{\omega_{\text{damp}}}{2} \times \min \left[1, \frac{\omega^2}{\omega_{\text{damp}}^2} \right]. \quad (25)$$

In the left column of Fig. 8, we show radial profiles of the local neutrino damping rate $\gamma_{\nu, \ell}$ for $\ell = 1 - 3$ waves at 225 ms, 349 ms, 475 ms, and 599 ms after core bounce.

The wave flux, propagating from the outer boundary of the

inner convective region (r_{con}) out towards the shock, is attenuated by a factor $e^{-x(\leq r)}$ after travelling to radius r , where $x(\leq r)$ is defined

$$x(\leq r) = \int_{r_{\text{con}}}^r \frac{dr' 2\gamma_{\nu}(r')}{v_{\text{gr}}}. \quad (26)$$

Here, $v_{\text{gr}} = |\omega/k_r|$ is the waves' group velocity. In the right column of Fig. 8, we show radial snapshots of the cumulative damping experienced, $x(\leq r)$, for $\ell = 1 - 3$ waves at 225, 349, 475, and 599 ms post-bounce.

We see that damping rates are typically largest in the outer PNS for all $\ell = 1 - 3$ waves. This makes sense, as neutrino cooling rates are largest in the outer PNS, and the neutrino damping operates in the optically thin limit. While optically thick wave damping in the inner core can be important at early times, this does not affect the outgoing waves of interest here. Neutrino damping becomes less important near the shock because the neutrino emissivities become smaller. Although outgoing waves can be rapidly damped in the outer PNS, their large group velocities prevent their attenuation factors $x(\leq r)$ from greatly exceeding unity.

The total fraction of unattenuated wave energy (i.e., the fraction of wave energy not lost to neutrino damping in travelling from the PNS out to the shock) is shown as a function of time in Fig. 9 for $\ell = 1 - 3$ waves. We expect neutrino damping to be somewhat important, with a moderate fraction of the wave energy lost within and below the gain region through neutrino emission. We discuss the ramifications of this, in addition to other potential concerns, in Section 6.

5.2 Non-linear effects

Waves excited by convection will continue to propagate inside the PNS until their energy is dissipated as heat. In the absence of damping, the wave displacement ξ (dependent on the total wave energy) grows as the waves propagate outwards into regions with lower density, and non-linear effects may quickly become non-negligible. A useful measure of non-linearity for both gravity waves and acoustic waves is the dimensionless quantity $|\mathbf{k} \cdot \xi| \sim |k_r \xi_r|$. Previous work (e.g., [Barker & Ogilvie 2011](#)) has shown that as $|k_r \xi_r| \rightarrow 1$, gravity waves overturn via stratification and break, losing energy via Kelvin-Helmholtz instabilities. As acoustic waves enter the non-linear regime, energy is lost as the waves self-shock and dissipate.

In the limit of no damping, it can be shown that the wave amplitude $|\xi|$ associated with energy flux L_{trans} is approximately ([Fuller & Ro 2018](#))

$$|\xi| \approx \left[\frac{L_{\text{trans}}}{4\pi\rho r^2 \omega^2 v_{\text{gr}}} \right]^{1/2}. \quad (27)$$

Since gravity waves propagate in the inner PNS and mantle before coupling to acoustic waves near the post-shock gain region, we consider both these cases in turn.

For gravity waves, the wave amplitude is $|\xi| \sim (|k_r/k_{\perp}|)\xi_r$, and the group velocity is $v_{\text{gr}} \sim \omega^2 r / (N\sqrt{\ell(\ell+1)})$. For low- ℓ gravity waves, the appropriate non-linearity measure thus follows

$$|k_r \xi_r|_{\text{grav}, \ell} \approx \left[\frac{L_{\text{trans}, \ell} N (\sqrt{\ell(\ell+1)})^3}{4\pi\rho r^5 \omega^4} \right]^{1/2}. \quad (28)$$

For acoustic waves, the wave amplitude is $|\xi| \sim \xi_r$, and the group

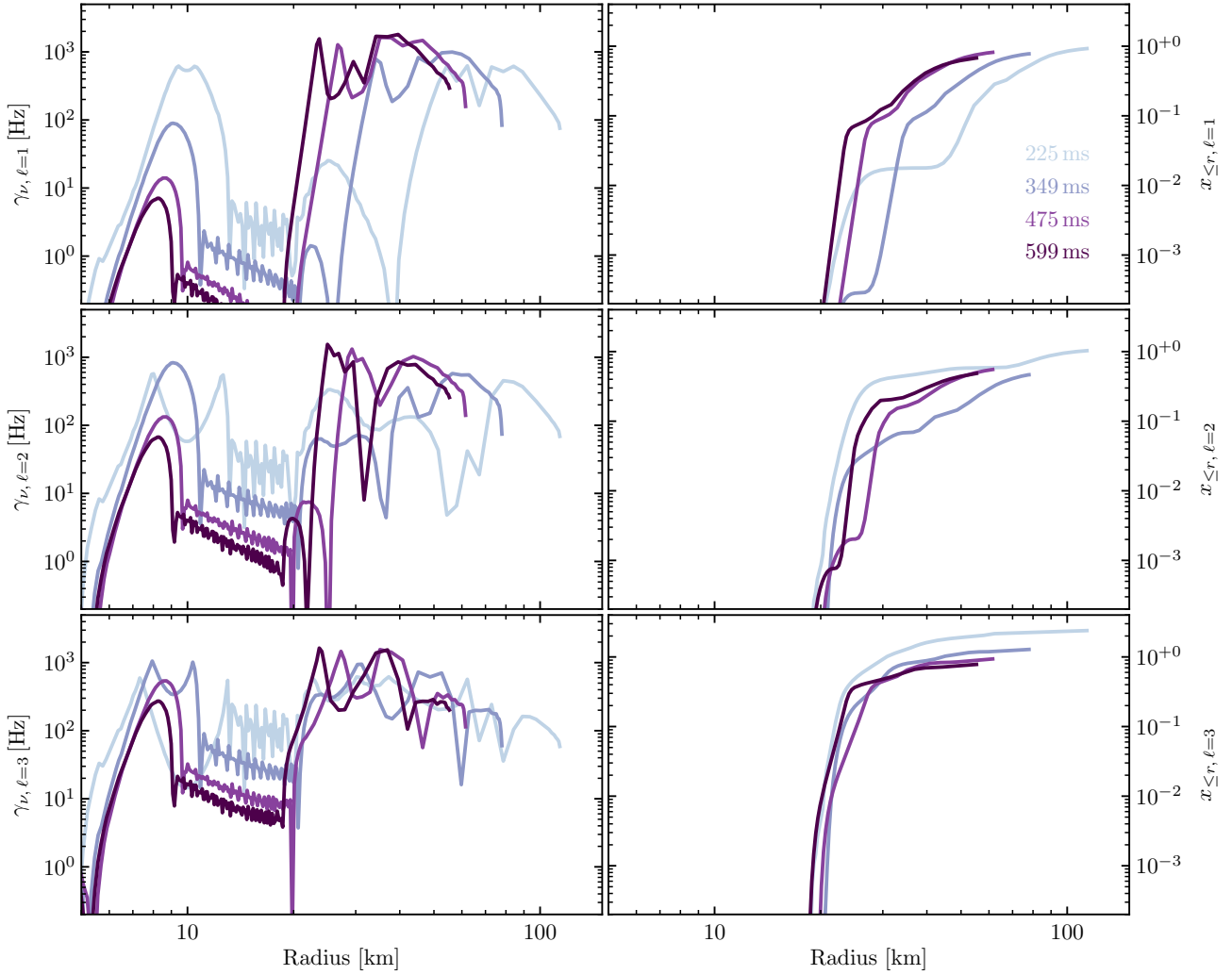


Figure 8. Snapshots of the local damping rate from neutrino diffusion γ_ν (left column), and the cumulative damping incurred by waves $x(\leq r)$ while propagating out from the outer edge of the inner PNS convective region r_{con} to radius r (right column). In each panel, radial traces are shown at 225 ms (in light blue), 349 ms (in lavender), 475 ms (in rich lilac), and 599 ms (in aubergine) for $\ell = 1$ (top panels), $\ell = 2$ (centre panels), and $\ell = 3$ (bottom panels) waves.

velocity is $v_{\text{gr}} = c_s$. It follows that, for low- ℓ acoustic waves,

$$|k_r \xi_r|_{\text{ac}, \ell} \approx \left[\frac{L_{\text{trans}, \ell}}{4\pi \rho r^2 c_s^3} \right]^{1/2}. \quad (29)$$

In Fig. 10, we show radial snapshots of $|k_r \xi_r|_\ell$ for $\ell = 1 - 3$ waves at 225 ms, 349 ms, 475 ms, and 599 ms after core bounce. Throughout the PNS for the duration of the simulation, $|k_r \xi_r|_\ell \ll 1$ for $\ell = 1$ waves. On approach to the gain region, $|k_r \xi_r|_\ell \sim 0.1$ for $\ell = 2$ and $\ell = 3$ waves. In the PNS core at early times, non-linear effects may be important for gravity waves. This suggests that waves propagating through the inner core are moderately non-linear, and may lose some fraction of their energy to non-linear dissipative effects. As we don't take their energy into account when calculating L_{trans} , such dissipation will not affect our main result, but could limit the contribution of such waves to any excess flux above L_{trans} . The main result is that no waves are in the strongly non-linear regime ($|k_r \xi_r|_\ell > 1$), so we do not expect rapid wave damping due to breaking or shock formation. We do find moderately non-linear amplitudes ($|k_r \xi_r|_\ell \gtrsim 0.1$) just below the shock, which could cause some wave damping there. When a successful explosion develops,

the shock moves out to lower densities, and it is much more likely that acoustic waves will become strongly non-linear, forming weak shocks and depositing their energy as heat within the PNS wind.

It is also important to address the possibility of non-linear three-mode coupling and whether this can quench the wave energy transport, as discussed by Weinberg & Quataert (2008). The primary waves excited by convection are low-order (0-2 radial nodes, $l = 1 - 3$) gravity waves in the outer PNS, whereas the acoustic mechanism involves low-order gravity modes in the inner PNS. Due to neutrino damping in the outer PNS, the outgoing convectively excited waves have low quality factors $Q \sim 3$ (see Fig. 9), and there are few daughter modes with frequencies $\omega_d \sim \omega_{\text{wave}}/2$ with which to resonantly couple. Mode coupling likely occurs in the non-resonant limit given by equation 2 of Weinberg & Quataert (2008), and hence we expect saturation energies of $E_{\text{sat}} \sim 10^{49}$ erg. In contrast to lower frequency modes trapped in the inner core, the gravity waves we consider traverse the outer PNS in a wave crossing time $t_{\text{cross}} \sim 5$ ms. The maximum rate at which the oscillating PNS can radiate energy in acoustic waves is $\dot{E} \sim E_{\text{sat}} T^2 / t_{\text{cross}} \sim 10^{51}$ erg s^{-1} for a transmission coefficient $T_\ell^2 = 0.5$. As a consequence, our computed energy fluxes are at the limit where non-linear coupling may affect

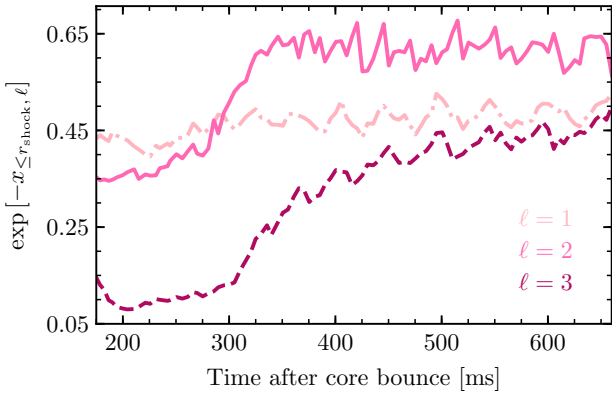


Figure 9. Temporal evolution of the fraction of wave luminosity not attenuated through neutrino damping (as measured just below the shock) with post-bounce time for $\ell = 1$ (dash-dotted light pink line), $\ell = 2$ (solid hot pink line), and $\ell = 3$ (dashed dark pink line) waves.

our results, but we do not expect non-linear suppression far below our estimates.

It is worth noting that the wave crossing time is only a few times larger than the wave oscillation periods, and comparable to the daughter mode periods. Hence, we consider it unlikely that non-linear coupling can dissipate the waves faster than the wave crossing time, and thus unlikely it can strongly attenuate the gravity waves before they transition into acoustic waves. This is an important distinction from lower frequency waves or modes trapped in the inner core, which must undergo many more oscillation cycles before their energy leaks out into the envelope.

Our estimates of wave heating are lower limits in the sense that they do not allow for gravity waves to reflect multiple times within the PNS before tunnelling into outgoing acoustic waves. In the absence of damping, multiple reflections could allow the acoustic wave energy flux to approach L_{waves} (Equation 3) rather than $L_{\text{waves}} T_{\ell}^2$. Based on the calculations above, however, non-linear coupling likely can prevent gravity waves from reflecting many times and accumulating energy in the outer PNS. With this in mind, it is unlikely that multiple reflections would greatly increase the wave heating rates.

5.3 Impact of waves on shock revival

Under the assumption that any wave energy lost to neutrinos free-streams out through the shock and escapes, an approximate lower limit on the wave energy heating rate in the post-shock region may be obtained simply by multiplying the wave transmission rate by the fraction not attenuated by neutrino damping. Explicitly, an estimate for the corrected heating rate L_{heat} is just

$$\begin{aligned} L_{\text{heat}} &= \sum_{\ell=1}^{\ell_c} L_{\text{trans}} \exp[-x_{\ell}] , \\ &= \sum_{\ell=1}^{\ell_c} L_{\text{heat}, \ell} . \end{aligned} \quad (30)$$

In the top panel of Fig. 11, we show the wave energy heating rate in the post-shock region as a function of time for $\ell = 1 - 3$ waves, in addition to the total heating rate summed over all excited angular modes. While slightly reduced relative to Fig. 7, we see that corrected wave heating rates are still expected to be substantial, with

typical values $L_{\text{heat}} \sim 4 - 10 \times 10^{50} \text{ erg s}^{-1}$ in wave power reaching the shock over the course of the simulation.

Exactly what happens as the waves reach the shock is complicated, but in general, downward reflection of the waves at the shock is expected. Acoustic waves are reflected at the discontinuity in density, entropy, and flow velocity, due to the supersonic inflow velocity above the shock. Generally speaking, acoustic waves here are partially reflected (to inwardly propagating acoustic waves) and partially transformed into vorticity and entropy waves through perturbation of the shock. Wave amplitudes can be augmented by tapping the kinetic energy of mass falling onto the shock, hence we expect the wave pressure calculations below to be conservative estimates. The interaction of outgoing acoustic waves with the stalled shock has been studied extensively in the context of the SASI (see, e.g., Foglizzo et al. 2007; Foglizzo 2009; Guilet et al. 2010; Guilet & Foglizzo 2012), but the particulars of the wave-shock interaction are beyond the scope of this study and left to future work. We also direct the interested reader to work by Abdikamalov et al. (2016), Huete et al. (2018), and Abdikamalov et al. (2018) for discussions on the interaction of waves with the stalled shock.

The momentum flux carried by the acoustic waves is imparted onto the shock as they reflect at it, just as photons impart momentum when they reflect at a surface. The waves therefore exert pressure on the shock, and a useful figure of merit to consider is the ratio of wave pressure P_{waves} to total fluid pressure at the shock. The momentum flux in acoustic waves is $L_{\text{waves}}/(2c_s)$, and thus the wave pressure can be estimated from the heating rate;

$$P_{\text{waves}} = \frac{L_{\text{heat}}}{4\pi r^2 c_s} , \quad (31)$$

where we employ the energy transport rate as computed above, corrected for the effects of neutrino damping.

In the lower panel of Fig. 11, we show the ratio of wave pressure to total pressure P_{waves}/P as a function of time. We show this quantity as measured in two places; just exterior to the entropy discontinuity marking the shock (a lower bound), in addition to the wave turning point where $\mathcal{M} = 1$ (an upper bound). Below the entropy discontinuity, we see wave pressure may account for over 15 per cent of the total pressure after 325 ms post-bounce, falling to ~ 5 per cent by the end of our simulation. In contrast, where $\mathcal{M} = 1$, in excess of 20 per cent of the total pressure is seen in waves from early times, rising to a maximum of $\sim 30 - 45$ per cent of the total pressure contributed in waves between 300 and 450 ms post-bounce. Between 500 ms through the end of the simulation, wave pressure ratios around ~ 25 and 35 per cent are consistently seen. We believe these estimates are relatively conservative, as wave pressure behind the shock may build up over time as a consequence of multiple interactions facilitated by wave reflection and/or multiple advective-acoustic cycles, similar to the SASI.

6 DISCUSSION

6.1 Implications for CCSN explosions

It is important to distinguish our work from the so-called acoustic mechanism (Burrows et al. 2006a,b), as also discussed in Section 2. In the acoustic mechanism, PNS oscillations are driven by asymmetric accretion onto the outer PNS, or by the SASI (Yoshida et al. 2007). These mechanisms essentially transfer kinetic energy from the accretion flow into the PNS and then back out toward the gain region, so there is no net transfer of energy from the PNS core outward. In our mechanism, wave energy excited by core convection is

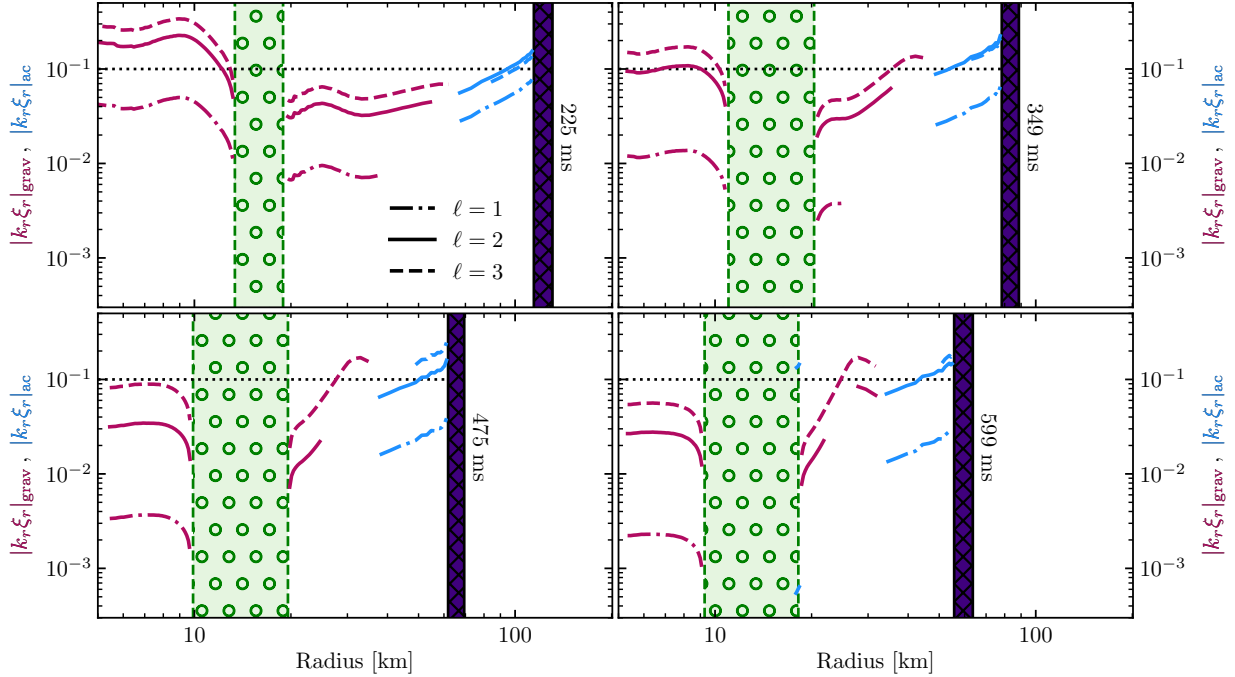


Figure 10. Radial profiles of dimensionless quantity $|k_r \xi_r|_\ell$ for $\ell = 1$ (dash-dotted line), $\ell = 2$ (solid line), and $\ell = 3$ (dashed line) waves at 225 ms (top left-hand panel), 349 ms (top right-hand panel), 475 ms (bottom left-hand panel), and 599 ms (bottom right-hand panel) after core bounce. Lines are shown in deep pink where gravity waves propagate ($\omega_{\text{con}} < N, L_\ell$), and shown in blue where acoustic waves travel ($\omega_{\text{con}} > N, L_\ell$). Regions in which the waves are evanescent (i.e., where $N < \omega_{\text{con}} < L_\ell$ or $L_\ell < \omega_{\text{con}} < N$) are left blank. For each snapshot, the inner convective region is shown in green with circled hatch, while the shock is shown in deep purple with crossed hatch. In each panel, we overlay dotted lines at $|k_r \xi_r|_\ell = 0.1$, beyond which non-linear effects may be important for the wave dynamics.

nearly independent of the accretion rate or asymmetry. Unlike the acoustic mechanism, the mechanism considered here can draw from the larger reservoir of PNS core binding energy ($E \sim 5 \times 10^{53}$ erg), albeit inefficiently. More importantly, wave excitation can persist for as long as the inner convection zone exists, which is likely for several seconds after core bounce (Burrows 1987; Roberts 2012b). Consequently, wave power generated in this scenario could contribute to the explosion power for long periods of time, even after the explosion has been fully launched and accretion power is negligible.

The extent to which acoustic energy aids explosion energy was studied in detail by Harada et al. (2017). On its own, acoustic power nearing 10^{52} erg is required to drive an explosion, which is unlikely to be generated by PNS core convection. However, in realistic models with neutrino luminosities of several 10^{52} erg s $^{-1}$, less than 10^{51} erg s $^{-1}$ of wave power could have a large effect, especially at late times when the mass accretion rate has declined. Hence, our predicted wave energy fluxes of $\sim 10^{51}$ erg s $^{-1}$ could play a pivotal role in shock revival for some supernovae.

Another important effect of waves may be late time (beyond ~ 500 ms) energy deposition in the PNS wind. Once the shock has been driven to large radii, the waves will steepen into shocks as they propagate into the low-density PNS wind (see Roberts 2012a), thereby thermalizing their energy in the inner explosion ejecta. Extrapolating Fig. 11 to late times, wave power of nearly 10^{51} erg s $^{-1}$ may be sustained for more than a second after bounce, potentially contributing as much as $\sim 10^{51}$ erg to the explosion energy. While some of this energy may well be lost to neutrino cooling, late-time wave energy deposition could significantly contribute to the final explosion energy. In light of the very low explosion energies

($E_{\text{exp}} \sim \text{few} \times 10^{50}$ erg) currently reached at end of many CCSN simulations, this effect seems especially important. The extent to which wave effects will contribute to the explosion energy at late times will depend on how efficiently convectively excited gravity waves are transmitted into outgoing acoustic waves. This efficiency is dependent on the structure of the outer PNS at late times, which will be quite different in the case of a successful explosion. As our simulations, which do not explode, cannot be used to compute this efficiency, we hope to quantify late time wave heating rates in future work.

A crucial implication of our study is that CCSN simulations that do not resolve the dynamics within the inner 20 km of the PNS may be missing an important source of explosion energy because they will not capture the effects of waves excited by the inner PNS convection zone. Indeed, many 3D and/or long-running simulations (see, e.g., Müller 2015b, 2017; Müller et al. 2019) evolve the inner PNS in spherical symmetry to allow for longer time-steps to be taken. The impact of this cut on the ability of a given simulation to resolve PNS convection and associated wave heating is dependent on the boundary criterion employed. Often, a density cut at $\rho \sim 5 \times 10^{11}$ g cm $^{-3}$ is chosen, such that higher densities are evolved in spherical symmetry. As can be seen from Fig. 3, this corresponds to a radial cut exterior to ~ 20 km and, as such, simulations employing this technique would miss the effect of waves excited by PNS convection and associated heating. Other simulations employing instead an explicit radius cut (often around ~ 10 km) should indeed resolve some of the convection and waves, but it is not clear how the dynamics would be affected by imposing an artificial inner boundary to the PNS convective zone, particularly at later times. Other simulations (e.g., Burrows et al. 2019; Vartanyan et al. 2019)

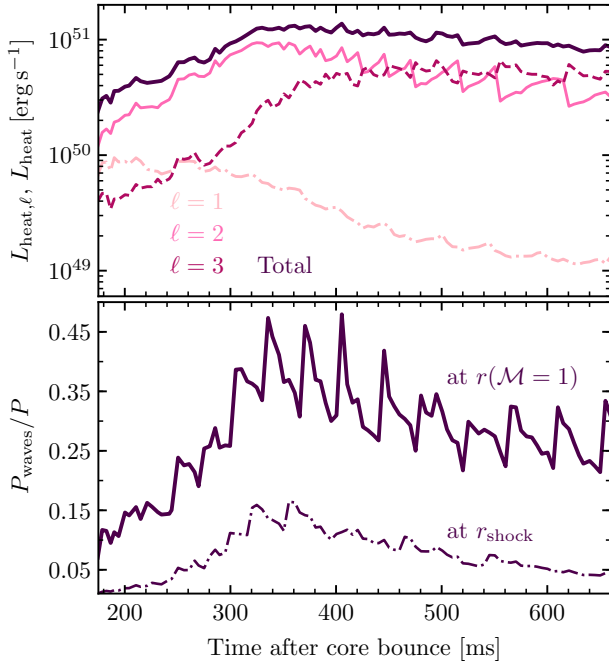


Figure 11. (Top panel) Temporal evolution of the net heating rates corrected for neutrino damping $L_{\text{heat},\ell}$ in $\ell = 1$ (dash-dotted light pink line), $\ell = 2$ (solid hot pink line), and $\ell = 3$ (dashed deep pink line) waves. The total net heating rate L_{heat} , summed over excited modes, is overlaid with a deep purple line. (Bottom panel) The ratio of the wave pressure (summed over excited modes) to the total pressure P_{waves}/P as a function of time, as measured where the Mach number $\mathcal{M} = 1$ (thick deep purple line), and immediately below the shock (thin dot-dashed deep purple line).

do resolve the dynamics of the inner PNS, though it is still not clear whether the 0.5 km resolution is sufficiently fine to accurately capture the effects of convective wave excitation and propagation. To help quantify the effects of waves, it would be interesting to compare simulations that evolve the inner PNS both with and without spherical symmetry. If waves are contributing to the explosion, we expect simulations that do resolve the dynamics of the inner PNS to explode more easily and with larger energies.

Energy fluxes from non-radial oscillations can be computed in simulations via

$$L_{\text{waves}} = \int dS \delta P \delta v_r. \quad (32)$$

Here, the integral is taken over a spherical surface area S , while δP and δv_r are the non-radial components of the pressure and radial velocity perturbations, respectively. Care should be taken to distinguish the upward wave energy flux from the downward energy and mass flux due to accretion. Müller (2015b) examined the *downward* energy flux of gravity waves that are excited by the *outer* convection zone, finding in 2D simulations downward energy fluxes as large as a few $\times 10^{50}$ erg s $^{-1}$, though their 3D simulations find much smaller downward energy fluxes due to less vigorous and less coherent convective motions. However, as those simulations did not resolve the inner PNS, the upward energy flux due to gravity waves excited by the inner PNS convection zone would have been missed. In general, both types of waves are expected to be present.

Gravity waves excited by PNS convection may be present in some simulations even if it is not recognized or discussed in corresponding papers. We expect non-radial horizontal motions of $\sim 10^3 - 10^4$ km s $^{-1}$ (with somewhat smaller radial motions) due

to gravity waves in the outer stably stratified region of the PNS, with larger motions at larger radii where the material is less dense. In the outer gravity wave cavity, the waves of interest have only one or two nodes and, hence, they may not appear particularly wavelike in simulations, perhaps instead resembling a large-scale ringing of the PNS. We note that gravity waves have opposite radial group and phase velocities, hence waves that carry energy upward have phases that propagate *downward*, which could easily be mistaken for downward propagating waves excited by convection and non-radial accretion from the overlying gain region. It is also possible that some of the vigorous motion in the gain region, usually attributed to neutrino-driven convection, could be caused partially by acoustic waves emerging from below.

Using simulations that resolved PNS convection, Andresen et al. (2017) found that inner PNS convection does indeed excite waves (although they did not quantify the hydrodynamic energy flux), and that these PNS motions can contribute to the gravitational wave (GW) emission from CCSNe. Using the same runs as Burrows et al. (2019), Radice et al. (2019) found that motions in the gain region helped excite fundamental and g-mode oscillations of the PNS, which dominated the GW emission found by their simulations. Torres-Forné et al. (2019b,a) found very similar results. The peak GW frequencies they find are similar but slightly larger than the gravity waves we expect to be excited by convection in the PNS mantle. As fundamental PNS modes are excited by waves from the outer convection zone (behind the shock) at early times (from ~ 100 ms post-bounce), this higher frequency emission dominates the GW spectrum because the energy flux in GWs is strongly dependent on frequency ($\dot{E}_{\text{GW}} \propto \omega^6$). At late times, after neutrino heating has died down, it is possible that PNS oscillations excited by PNS convection (which will persist for several seconds as the PNS cools and contracts) could dominate the GW emission. Indeed, if true, this could mirror the scenario we are proposing in this paper; at early times, neutrino heating may dominate the explosion dynamics (and the GW signature), but waves excited by convection in the PNS mantle could contribute significantly to explosion dynamics, PNS evolution, and consequently the GW emission, beyond a few hundred milliseconds post-bounce. Further investigations into wave heating from PNS convection will require simulations that resolve the PNS to evolve it from formation out to several seconds after core bounce.

Ours is not the first work to consider the impacts of convectively excited waves on CCSNe. Metzger et al. (2007) examined the impacts of convectively excited Alfvén waves on r -process nucleosynthesis in PNS winds. Wave heat deposited at the base of the PNS wind can help drive it outward more rapidly, such that it maintains lower Y_e and produces more r -process elements. Metzger et al. (2007) found Alfvén wave heating may be important, but only for protomagnetar-type remnants with magnetic fields on the order $B \sim 10^{15}$ G. Even then, they estimated wave heating rates of only $L \lesssim 10^{49}$ erg s $^{-1}$, roughly two orders of magnitude smaller than the wave heating estimates we predict here. Suzuki et al. (2008) found that Alfvén waves could revive the shock only for remnants with exceptionally large field strengths ($B \gtrsim 2 \times 10^{15}$ G) and perturbation amplitudes. Roberts (2012a) considered the impact of gravito-acoustic waves excited by PNS convection on nucleosynthesis in neutrino driven winds. There, it was found that energy deposition by gravito-acoustic waves could strongly impact the dynamics of the wind, but the impact on nucleosynthesis depended strongly on the radius at which the acoustic waves steepened into shocks. Under favourable conditions, this extra heating resulted in production of the r -process in mildly neutron-rich conditions. Based on that

work and the results found here, we believe that waves hydrodynamically excited by PNS convection are usually more important for both the explosion and nucleosynthesis in the neutrino driven wind than Alfvén waves. In light of our results, the effect of wave heating on nucleosynthesis in the neutrino-driven wind should be reinvestigated.

6.2 Uncertainties

As explained in Section 4, we make the approximation that all wave flux excited by PNS convection is at the convective overturn frequency ω_{con} and that the angular wave spectrum is flat in modes $\ell \in [1, \dots, \ell_c]$. While the spectral behaviour of waves excited in this way is not well understood, our prescription is rooted in the assertions made in Goldreich & Kumar (1990), Kumar et al. (1999), and Lecoanet & Quataert (2013), on the basis of bulk Reynolds stresses driving convective wave excitation. The propagation path of the excited waves, as shown in Fig. 5, is clearly frequency dependent, a statement we have quantified with the fraction of wave flux transmitted from gravity waves to acoustic waves in the outer PNS as a function of frequency shown in Fig. 6. Based on these figures, it would appear that emission at higher frequencies, as argued for by Rogers et al. (2013) and Pinçon et al. (2016) on the basis of plume incursion driving convective wave excitation, may slightly increase the fraction of transmitted wave flux. As a consequence, despite their somewhat crude and uncertain nature, we believe our estimates of the wave flux excited by PNS convection are conservative. More importantly, we see from Fig. 5 that the transmitted wave flux may be higher or lower at different wave frequencies for different values of ℓ , but integrating over a broad frequency spectrum will yield wave fluxes of similar magnitude to our rough estimates.

Neutrino damping likely has a substantial impact on wave heating rates. As we have shown in Fig. 9, a moderate fraction of the wave flux is likely to be damped away through increased neutrino energy losses in the marginally optically thin region around the neutrinosphere. Our estimates of neutrino damping, admittedly somewhat crude, use a WKB approximation for the waves (which is only marginally valid for low-order gravity waves), and do not accurately predict neutrino losses where the optical depth across a wavelength is near unity. Hence, a more careful assessment of neutrino damping of waves from CCSN simulations is warranted.

Given all emission at ω_{con} with a flat angular spectrum in $\ell \in [1, \dots, \ell_c]$, strong non-linear effects are likely to be important only for gravity waves in the PNS core at early times, and perhaps additionally for acoustic waves in the gain region on very close approach to the shock. While non-linear damping in the core may prevent wave energy emitted into the core from escaping, the estimates for L_{trans} we present consider only outwardly propagating waves, and thus can only be increased by wave flux escaping from the inner core. Our estimates suggest that non-linear three-mode coupling, as discussed by Weinberg & Quataert (2008), is marginally important for the waves we consider. Waves with lower ω and higher-order angular wavenumber ℓ are more susceptible to non-linear effects due to their larger radial wavenumbers $|k_{r,\ell}|$ and slower group velocities v_{gr} . If convection excites waves at predominantly lower frequencies (or higher ℓ than our estimates), three-mode coupling could reduce the wave flux transmitted into acoustic waves. Alternatively, convective excitation at higher frequency or lower ℓ could increase the transmitted wave flux. In the latter case, increased transmission of acoustic wave flux will increase the non-linearity of acoustic waves in the gain region, increasing the likelihood of wave damping through weak shock formation.

Beyond the points already highlighted here and previously alluded to, a crucial limitation underscoring this work is the failure of our simulations to explode. The thermodynamic structure of the accreting PNS, particularly in the immediate post-shock region, will be altered in the case of a successful explosion. Although this is unlikely to impact the development or persistence of convection in the PNS mantle over the time-scales considered in this study, the propagation of waves through the outer PNS and the gain regions is likely to be impacted. A quantitative evaluation of the effect on wave pressure and corrected heating rates are beyond the scope of this study, but should be considered in future work.

7 CONCLUSION

In the first few seconds after core collapse, energy transport by convectively excited waves from the inner PNS toward the shock may have a substantial impact on the outcome of core collapse and explosion energy. To quantify wave energy transport, we have modelled the core collapse of a $15 M_{\odot}$ progenitor and followed post-bounce evolution for 660 ms. We used a spherically symmetric, general relativistic hydrodynamics code employing a mixing length theory prescription for convection (Roberts 2012a; Roberts et al. 2012) to estimate wave generation rates, analyse wave propagation within the PNS, and compute wave energy fluxes behind the stalled shock.

Convection develops in the PNS mantle after around 200 ms post-bounce due to deleptonization and entropy changes as the PNS contracts. We see convective luminosities of $L_{\text{con}} \sim 10^{53} \text{ erg s}^{-1}$ across the inner convective region, of which a few $10^{51} \text{ erg s}^{-1}$ is expected to be radiated outwards as gravity waves from the outer edge with frequencies near the convective turnover frequency, which we estimate to increase from $\sim 10^3$ to $\sim 4 \times 10^3 \text{ rad s}^{-1}$ over the course of the simulation. Because the convectively excited gravity waves encounter a relatively narrow evanescent region between the PNS and the gain region, a large fraction ($T_{\ell}^2 \sim 1/3$) of their energy is transmitted into acoustic waves that propagate out toward the shock. In the post-shock region, we find net wave energy transport rates slightly exceeding $10^{51} \text{ erg s}^{-1}$ sustained through the end of the simulation.

Neutrino damping of acoustic waves in the outer PNS is likely to be significant, with a moderate fraction of wave energy dissipated due to escaping neutrinos. Accounting for the effects of neutrino damping, we still find wave heating rates of nearly $10^{51} \text{ erg s}^{-1}$ sustained through the end of the simulation (c.f. Fig. 11). While we do not expect non-linear effects to drastically alter our results, steepening of acoustic waves could cause energy deposition in the post-shock region, especially once the explosion commences and the shock moves outward. Non-linear three-mode coupling in the outer PNS could moderately reduce the amount of wave energy escaping toward the gain region, particularly if the spectrum of the waves excited by convection peaks at lower frequencies than we have assumed, though we find it unlikely to drastically affect our results.

Although we do not expect wave energy transport to be the primary driver of the supernova explosion, our study here shows that its impact is expected to be highly significant, contributing as much as 40 per cent of the pressure upon the shock. Since many configurations of core collapse exist very close to the threshold between collapse and explosion (see, e.g., Melson et al. 2015; Müller et al. 2017), waves may play a crucial role in numerous events. Furthermore, since wave heating extends to late times (beyond 500 ms

post-bounce) and falls off at a slower rate than neutrino heating, wave energy may significantly contribute to the final energy of the explosion. Future simulations can better quantify the impact of waves, and we encourage CCSN modellers to attempt to resolve the inner PNS in order to capture wave excitation and propagation originating from convection in the PNS mantle. We also suggest a re-examination of the outgoing hydrodynamic energy flux from the PNS, as convectively excited waves could be present in some existing simulations, but may be unrecognised or even mistaken for downgoing waves.

The physics governing CCSNe is rich and diverse, encompassing turbulent hydrodynamic instabilities and complex radiative transfer of neutrinos. In the absence of unlimited computational resources, the extent to which these systems can be modelled is constrained by the approximations used to make such studies viable. Wave physics in itself is a complex field which is not fully understood, and thus our results are both estimative and subject to a number of uncertainties that have been outlined in this study and can be improved upon with further investigation. Nevertheless, it is clear that the accurate quantification of the impact of wave heating from PNS convection on the revival of the stalled supernova shock is vital to developing a comprehensive understanding of the CCSN explosion mechanism.

ACKNOWLEDGEMENTS

We acknowledge helpful discussions with T. Foglizzo, A. Harada, and E. Lentz of great benefit to this work. SEG thanks S. Nisanke, R. Wijers, the GRavitation AstroParticle Physics Amsterdam (GRAPPA) group, and the Anton Pannekoek Institute (API) for their hospitality at Universiteit van Amsterdam (UvA), where much of this work was carried out. This research is funded in part by an Innovator Grant from The Rose Hills Foundation, the Sloan Foundation through grant FG-2018-10515, and by the National Science Foundation under Grant No. NSF PHY-1748958.

Software: All figures presented in this paper were produced using PYTHON, MATPLOTLIB (Hunter 2007), NUMPY (Oliphant 2006; van der Walt et al. 2011), and SCIPY (Virtanen et al. 2020).

REFERENCES

- Abdikamalov E., et al., 2015, *ApJ*, **808**, 70
- Abdikamalov E., Zhakyslykov A., Radice D., Berdibek S., 2016, *MNRAS*, **461**, 3864
- Abdikamalov E., Huete C., Nussupbekov A., Berdibek S., 2018, arXiv e-prints, p. [arXiv:1805.03957](https://arxiv.org/abs/1805.03957)
- Alvan L., Brun A. S., Mathis S., 2014, *A&A*, **565**, A42
- Andresen H., Müller B., Müller E., Janka H.-T., 2017, *MNRAS*, **468**, 2032
- Barker A. J., Ogilvie G. I., 2011, *MNRAS*, **417**, 745
- Bethe H. A., Wilson J. R., 1985, *ApJ*, **295**, 14
- Bollig R., Janka H. T., Lohs A., Martínez-Pinedo G., Horowitz C. J., Melson T., 2017, *Phys. Rev. Lett.*, **119**, 242702
- Burrows A., 1987, *ApJ*, **318**, L57
- Burrows A., Livne E., Dessart L., Ott C. D., Murphy J., 2006a, *ApJ*, **640**, 878
- Burrows A., Reddy S., Thompson T. A., 2006b, *Nucl. Phys. A*, **777**, 356
- Burrows A., Vartanyan D., Dolence J. C., Skinner M. A., Radice D., 2018, *Space Sci. Rev.*, **214**, 33
- Burrows A., Radice D., Vartanyan D., 2019, *MNRAS*, **485**, 3153
- Burrows A., Radice D., Vartanyan D., Nagakura H., Skinner M. A., Dolence J. C., 2020, *MNRAS*, **491**, 2715
- Couch S. M., Ott C. D., 2015, *ApJ*, **799**
- Couch S. M., Chatzopoulos E., Arnett W. D., Timmes F. X., 2015, *ApJ*, **808**, L21
- Couston L.-A., Lecoanet D., Favier B., Le Bars M., 2018, *J. Fluid Mech.*, **854**, R3
- Dessart L., Burrows A., Livne E., Ott C. D., 2006, *ApJ*, **645**, 534
- Foglizzo T., 2009, *ApJ*, **694**, 820
- Foglizzo T., Galletti P., Scheck L., Janka H.-T., 2007, *ApJ*, **654**, 1006
- Fuller J., 2017, *MNRAS*, **470**, 1642
- Fuller J., Ro S., 2018, *MNRAS*, **476**, 1853
- Fuller J., Lecoanet D., Cantiello M., Brown B., 2014, *ApJ*, **796**, 17
- Fuller J., Cantiello M., Stello D., Garcia R. A., Bildsten L., 2015a, *Science*, **350**, 423
- Fuller J., Cantiello M., Lecoanet D., Quataert E., 2015b, *ApJ*, **810**, 101
- Goldreich P., Kumar P., 1990, *ApJ*, **363**, 694
- Guilet J., Foglizzo T., 2012, *MNRAS*, **421**, 546
- Guilet J., Sato J., Foglizzo T., 2010, *ApJ*, **713**, 1350
- Hanke F., Marek A., Müller B., Janka H.-T., 2012, *ApJ*, **755**, 138
- Harada A., Nagakura H., Iwakami W., Yamada S., 2017, *ApJ*, **839**, 28
- Huete C., Abdikamalov E., Radice D., 2018, *MNRAS*, **475**, 3305
- Hunter J. D., 2007, *CSE*, **9**, 90
- Janka H.-T., 2012, *Ann. Rev. Nuc. Par. Sci.*, **62**, 407
- Janka H.-T., Melson T., Summa A., 2016, *Ann. Rev. Nucl. Part. Sci.*, **66**, 341
- Kumar P., Talon S., Zahn J.-P., 1999, *ApJ*, **520**, 859
- Lattimer J. M., Douglas Swesty F., 1991, *Nucl. Phys. A*, **535**, 331
- Lecoanet D., Quataert E., 2013, *MNRAS*, **430**, 2363
- Lentz E. J., et al., 2015, *ApJ*, **807**, L31
- Meakin C. A., Arnett D., 2007, *ApJ*, **667**, 448
- Melson T., Janka H.-T., Bollig R., Hanke F., Marek A., Müller B., 2015, *ApJ*, **808**, L42
- Metzger B. D., Thompson T. A., Quataert E., 2007, *ApJ*, **659**, 561
- Mihalas B., Weibel-Mihalas B., 1984, *Foundations of Radiation Hydrodynamics*. Oxford Univ. Press
- Müller B., 2015a, *MNRAS*, **453**, 287
- Müller B., 2015b, *MNRAS*, **453**, 287
- Müller B., 2016, *PASA*, **33**, e048
- Müller B., 2017, *IAUS*, **329**, 17
- Müller B., Janka H.-T., 2014, *ApJ*, **788**, 82
- Müller B., Melson T., Heger A., Janka H.-T., 2017, *MNRAS*, **472**, 491
- Müller B., et al., 2019, *MNRAS*, **484**, 3307
- O'Connor E., et al., 2018, *J. Phys. G Nucl. Phys.*, **45**, 104001
- Oliphant T. E., 2006, *A guide to NumPy*. Trelgol Publishing, USA
- Ott C. D., Roberts L. F., da Silva Schneider A., Fedrow J. M., Haas R., Schnetter E., 2018, *ApJ*, **855**, L3
- Pinçon C., Belkacem K., Goupil M. J., 2016, *A&A*, **588**, A122
- Pons J. A., Reddy S., Prakash M., Lattimer J. M., Miralles J. A., 1999, *ApJ*, **513**, 780
- Quataert E., Shiode J., 2012, *MNRAS*, **423**, L92
- Radice D., Couch S. M., Ott C. D., 2015, *ComAC*, **2**, 7
- Radice D., Morozova V., Burrows A., Vartanyan D., Nagakura H., 2019, *ApJ*, **876**, L9
- Roberts L. F., 2012a, PhD thesis, University of California, Santa Cruz
- Roberts L. F., 2012b, *ApJ*, **755**, 126
- Roberts L. F., Shen G., Cirigliano V., Pons J. A., Reddy S., Woosley S. E., 2012, *Phys. Rev. Lett.*, **108**, 061103
- Roberts L. F., Ott C. D., Haas R., O'Connor E. P., Diener P., Schnetter E., 2016, *ApJ*, **831**
- Rogers T. M., Lin D. N. C., Lau H. H. B., 2012, *ApJ*, **758**, L6
- Rogers T. M., Lin D. N. C., McElwaine J. N., Lau H. H. B., 2013, *ApJ*, **772**, 21
- Schneider A. S., Roberts L. F., Ott C. D., 2017, *Phys. Rev. C*, **96**, 065802
- Schneider A. S., Roberts L. F., Ott C. D., O'Connor E., 2019, *Phys. Rev. C*, **100**, 055802
- Suzuki T. K., Sumiyoshi K., Yamada S., 2008, *ApJ*, **678**, 1200
- Talon S., Kumar P., Zahn J.-P., 2002, *ApJ*, **574**, L175
- Torres-Forné A., Cerdá-Durán P., Obergaulinger M., Müller B., Font J. A., 2019a, *Phys. Rev. Lett.*, **123**, 051102
- Torres-Forné A., Cerdá-Durán P., Passamonti A., Obergaulinger M., Font J. A., 2019b, *MNRAS*, **482**, 3967

- Vartanyan D., Burrows A., Radice D., Skinner M. A., Dolence J., 2019, *MNRAS*, **482**, 351
- Virtanen P., et al., 2020, *Nat. Methods*, **17**, 261
- Weinberg N. N., Quataert E., 2008, *MNRAS*, **387**, L64
- Woolsey S. E., Weaver T. A., 1995, *ApJS*, **101**, 181
- Yoshida S., Ohnishi N., Yamada S., 2007, *ApJ*, **665**, 1268
- van der Walt S., Colbert S. C., Varoquaux G., 2011, *Comput. Sci. Eng.*, **13**, 22

APPENDIX A: WAVE DAMPING VIA NEUTRINO DISSIPATION

Wave energy dissipation is expected to occur due to non-adiabatic corrections from neutrino emission. The energy loss rate per unit mass due to neutrino damping, $\dot{\epsilon}_\nu$, can be calculated as

$$\dot{\epsilon}_\nu = \delta T \delta \left(\frac{ds}{dt} \right)_\nu, \quad (\text{A1})$$

where δ denotes the Lagrangian variation of the following term, and

$$\left(\frac{ds}{dt} \right)_\nu = \sum_{\nu_i \in \{\nu_e, \bar{\nu}_e, \nu_x\}} \left(\frac{S_{\nu_i}}{T} - \frac{1}{n_B T} \left[\vec{\nabla} \cdot \vec{H}_{\nu_i} - \mu_{\nu_i} \vec{\nabla} \cdot \vec{F}_{\nu_i} \right] \right) \quad (\text{A2})$$

is the rate of change of the specific entropy s due to neutrino losses. Here, the source function S_{ν_i} , number flux F_{ν_i} , energy flux H_{ν_i} , and chemical potential μ_{ν_i} are distinct for each neutrino species ν_i . In equations (A2) and (A3), Boltzmann's constant $k_B \rightarrow 1$. The source function, which encompasses effects from both the emission and absorption of neutrinos of species ν_i , is defined

$$S_{\nu_i} = \frac{4\pi c}{n_B} \int_0^\infty \frac{d\omega}{(2\pi\hbar c)^3} \omega^3 \kappa_{\nu_i}^*(\omega) \times [f_{\nu_i, \text{eq}}(\omega, T, \mu_{\nu_i, \text{eq}}) - f_{\nu_i}(\omega)], \quad (\text{A3})$$

where $\kappa_{\nu_i}^*$ is the stimulated absorption opacity (with units of inverse length), f_{ν_i} is the neutrino distribution function, and $f_{\nu_i, \text{eq}}$ is the distribution function describing a hypothetical population of ν_i neutrinos in thermal and chemical equilibrium with the background medium, which takes the usual Fermi-Dirac form.

Generally speaking, the distribution functions for each neutrino population must be calculated from the Boltzmann equation. In the optically thin and optically thick limits, however, one can make approximations and compute $\dot{\epsilon}_\nu$ in terms of local thermodynamic quantities and their spatial gradients. We now discuss these cases in turn.

A1 Optically thick limit

In the optically thick (i.e. diffusive) limit, $f_{\nu_i} \rightarrow f_{\nu_i, \text{eq}}$ plus some small anisotropic correction. As such, neutrino emission and absorption are locally balanced and $S_{\nu_i} \rightarrow 0$.

As derived in Pons et al. (1999), the diffusive fluxes in this limit for neutrino species ν_i may be written in terms of the local temperature and neutrino degeneracy parameter ($\eta_{\nu_i} = \mu_{\nu_i}/T$) gradients:

$$\vec{F}_{\nu_i} = -\frac{cT^2}{6\pi^2(\hbar c)^3} \left[D_{3, \nu_i} \vec{\nabla} T + D_{2, \nu_i} T \vec{\nabla} \eta_{\nu_i} \right], \quad (\text{A4})$$

$$\vec{H}_{\nu_i} = -\frac{cT^3}{6\pi^2(\hbar c)^3} \left[D_{4, \nu_i} \vec{\nabla} T + D_{3, \nu_i} T \vec{\nabla} \eta_{\nu_i} \right], \quad (\text{A5})$$

where diffusion coefficients D_{n, ν_i} (essentially inverse Rosseland mean opacities) are defined

$$D_{n, \nu_i} = \int_0^\infty d\omega \frac{\omega^n f_{\nu_i, \text{eq}}(\omega) [1 - f_{\nu_i, \text{eq}}(\omega)]}{T^{n+1} [\kappa_{\text{abs}, \nu_i}^*(\omega) + \kappa_{\text{scat}, \nu_i}^*(\omega)]}, \quad (\text{A6})$$

and $\kappa_{\text{scat}, \nu_i}^*(\omega)$ here is the scattering transport opacity for neutrino species ν_i , with units of inverse length.

Diffusive losses here are dominated by neutral-current scattering of heavy-lepton neutrinos on nucleons. As the heavy-lepton chemical potential $\mu_{\nu_x} = 0$ everywhere, we see that

$$\left(\frac{ds}{dt} \right)_\nu \approx -\frac{1}{n_B T} \vec{\nabla} \cdot \vec{H}_{\nu_x}. \quad (\text{A7})$$

Using the diffusive approximations introduced above, the heavy-lepton neutrino energy flux \vec{H}_{ν_x} may be written

$$\vec{H}_{\nu_x} = -\frac{4cT^3}{6\pi^2(\hbar c)^3} D_{4, \nu_x} \vec{\nabla} T, \quad (\text{A8})$$

where the factor of four here in the numerator accounts for the summed flux over the four flavours encompassed by the heavy-lepton neutrino species, $\nu_x \in \{\nu_\mu, \bar{\nu}_\mu, \nu_\tau, \bar{\nu}_\tau\}$.

To compute D_{4, ν_x} , we consider the transport opacity for heavy-lepton neutrinos from neutral-current scattering on nucleons. Employing expressions from Sections 3.4 and 3.5 of Burrows et al. (2006a), we may write

$$\kappa_{\text{scat}, \nu_x}^*(\omega) \approx n_B \sigma_0 \left(\frac{\hbar\omega}{m_e c^2} \right)^2 C(Y_e). \quad (\text{A9})$$

Here, $\hbar\omega$ is the neutrino energy and $C(Y_e)$ encompasses coupling constants and composition effects:

$$C(Y_e) = \frac{1 + 5g_A^2}{6} \frac{1 - Y_e}{4} + \frac{(C'_V - 1)^2 + 5g_A^2 (C'_A - 1)^2}{6} Y_e. \quad (\text{A10})$$

Substituting this into the expression for D_{4, ν_x} and making the change of variables $\hbar\omega \rightarrow x = \omega/T$ yields

$$D_{4, \nu_x} \approx \frac{\pi^2 (m_e c^2)^2}{6 n_B \sigma_0 C(Y_e) T^2}, \quad (\text{A11})$$

where we employ the identity

$$\int_0^\infty dx \frac{x^2 e^x}{(e^x + 1)^2} = \frac{\pi^2}{6}. \quad (\text{A12})$$

The energy flux in heavy-lepton neutrinos naturally follows

$$\vec{H}_{\nu_x} \approx -\frac{c (m_e c^2)^2}{9 (\hbar c)^3 \sigma_0} \frac{T}{n_B C(Y_e)} \vec{\nabla} T, \quad (\text{A13})$$

from which we find

$$\left(\frac{ds}{dt} \right)_\nu \approx \frac{1}{n_B T} \frac{c (m_e c^2)^2}{9 (\hbar c)^3 \sigma_0} \times \left[\vec{\nabla} \left(\frac{T}{n_B C(Y_e)} \right) \cdot \vec{\nabla} T + \frac{T}{n_B C(Y_e)} \nabla^2 T \right]. \quad (\text{A14})$$

Taking now the Lagrangian variation of this expression and neglecting terms second-order and above in perturbations, we can write

$$\delta \left(\frac{ds}{dt} \right)_\nu \approx \frac{c (m_e c^2)^2}{9 (\hbar c)^3 \sigma_0} \frac{\nabla^2 \delta T}{n_B^2 C(Y_e)}, \quad (\text{A15})$$

$$\approx -\frac{c (m_e c^2)^2}{9 (\hbar c)^3 \sigma_0} \frac{k^2 \delta T}{n_B^2 C(Y_e)},$$

where we have employed the WKB approximation to substitute $\nabla^2 \delta T \rightarrow -k^2 \delta T$ and to ignore terms of lower order in k .

From here, the damping rate in neutrinos in the optically thick limit is just

$$\begin{aligned} \dot{\epsilon}_{\nu, \text{thick}} &= \delta T \delta \left(\frac{ds}{dt} \right)_{\nu}, \\ &\approx -\frac{c (m_e c^2)^2}{9 (\hbar c)^3 \sigma_0 n_B^2} \frac{k^2 \delta T^2}{C(Y_e)}. \end{aligned} \quad (\text{A16})$$

A2 Optically thin limit

In the optically thin limit, $f_{\nu_i}(\omega) \approx 0$, and the entropy evolution equation takes the simplified form

$$\left(\frac{ds}{dt} \right)_{\nu} = \sum_{\nu_i \in \{\nu_e, \bar{\nu}_e, \nu_x\}} \frac{\dot{\epsilon}_{\nu_i}}{T}, \quad (\text{A17})$$

where the neutrino emission rates $\dot{\epsilon}_{\nu_i}$ (with units of per second per baryon) are defined

$$\dot{\epsilon}_{\nu_i} = \frac{\hbar}{2\pi^2 n_B c^2} \int_0^{\infty} d\omega \frac{\omega^3 \kappa_{\nu_i}^*(\omega)}{e^{\hbar\omega/T - \eta_{\nu_i}} + 1}. \quad (\text{A18})$$

In this limit, losses are dominated by emission of ν_e and $\bar{\nu}_e$ neutrinos, driven by charged-current capture on nucleons. Explicitly, the relevant stimulated absorption opacities may be written

$$\begin{aligned} \kappa_{\nu_e}^*(\hbar\omega) &= n_B (1 - Y_e) \sigma_0 \left(\frac{1 + 3g_A^2}{4} \right) \left(\frac{\hbar\omega + \Delta_{np}}{m_e c^2} \right)^2 \\ &\times \left[1 + e^{-(\hbar\omega/T - \eta_{\nu_e, \text{eq}})} \right], \end{aligned} \quad (\text{A19})$$

$$\begin{aligned} \kappa_{\bar{\nu}_e}^*(\hbar\omega) &= n_B Y_e \sigma_0 \left(\frac{1 + 3g_A^2}{4} \right) \left(\frac{\hbar\omega - \Delta_{np}}{m_e c^2} \right)^2 \\ &\times \left[1 + e^{-(\hbar\omega/T + \eta_{\nu_e, \text{eq}})} \right], \end{aligned} \quad (\text{A20})$$

where $\Delta_{np} = (m_n - m_p) c^2$ is the energy-equivalent mass difference between neutrons and protons. Substituting these expressions into the formulae above and, once more, making the variable substitution $\omega \rightarrow x = \hbar\omega/T$, we find a total emissivity of the form

$$\dot{\epsilon}_{\nu_e + \bar{\nu}_e} \approx \frac{c\sigma_0}{8\pi^2 (\hbar c)^3 (m_e c^2)^2} C_{\nu_e + \bar{\nu}_e, \text{thin}} T^6, \quad (\text{A21})$$

where we have defined $C_{\nu_e + \bar{\nu}_e, \text{thin}}$, which encompasses the relevant coupling constants and compositional effects, as

$$\begin{aligned} C_{\nu_e + \bar{\nu}_e, \text{thin}} &= (1 + 3g_A^2) \\ &\times \left[Y_e \int_{\Delta_{np}/T}^{\infty} dx x^5 \left(1 - \frac{\Delta_{np}}{xT} \right)^2 \frac{1 + e^{-x - \eta_{\nu_e, \text{eq}}}}{1 + e^{x + \eta_{\nu_e, \text{eq}}}} \right. \\ &\left. + (1 - Y_e) \int_0^{\infty} dx x^5 \left(1 + \frac{\Delta_{np}}{xT} \right)^2 \frac{1 + e^{-x + \eta_{\nu_e, \text{eq}}}}{1 + e^{x - \eta_{\nu_e, \text{eq}}}} \right], \end{aligned} \quad (\text{A22})$$

Returning now to calculate the energy loss rate, we have

$$\begin{aligned} \dot{\epsilon}_{\nu_e + \bar{\nu}_e, \text{thin}} &\approx \delta \left(\frac{\dot{\epsilon}_{\nu_e + \bar{\nu}_e}}{T} \right) \delta T, \\ &\approx \dot{\epsilon}_{\nu_e + \bar{\nu}_e} \frac{\delta T}{T} \left[\left(\frac{\partial \log \dot{\epsilon}_{\nu_e + \bar{\nu}_e}}{\partial \log T} \right)_{n_B, Y_e} \frac{\delta T}{T} \right. \\ &\quad + \left(\frac{\partial \log \dot{\epsilon}_{\nu_e + \bar{\nu}_e}}{\partial \log n_B} \right)_{T, Y_e} \frac{\delta n_B}{n_B} \\ &\quad \left. + \left(\frac{\partial \log \dot{\epsilon}_{\nu_e + \bar{\nu}_e}}{\partial \log Y_e} \right)_{T, n_B} \frac{\delta Y_e}{Y_e} \right], \\ &\approx \dot{\epsilon}_{\nu_e + \bar{\nu}_e} \frac{\delta T}{T} \left[6 \frac{\delta T}{T} - \frac{\delta Y_e}{Y_e} \right], \end{aligned} \quad (\text{A23})$$

Neglecting composition effects to focus instead on the much stronger temperature dependence, we find

$$\dot{\epsilon}_{\nu_e + \bar{\nu}_e, \text{thin}} \approx \frac{3c\sigma_0}{4\pi^2 (\hbar c)^3 (m_e c^2)^2} C_{\nu_e + \bar{\nu}_e, \text{thin}} T^4 \delta T^2. \quad (\text{A24})$$

This paper has been typeset from a $\text{\TeX}/\text{\LaTeX}$ file prepared by the author.